



# The applications of solid-state NMR and MRI techniques in the study of rechargeable sodium-ion batteries



Peizhao Shan<sup>a</sup>, Junning Chen<sup>a</sup>, Mingming Tao<sup>a</sup>, Danhui Zhao<sup>a</sup>, Hongxin Lin<sup>a</sup>, Riqiang Fu<sup>b</sup>, Yong Yang<sup>a,\*</sup>

<sup>a</sup>State Key Laboratory for Physical Chemistry of Solid Surfaces, and Department of Chemistry, College of Chemistry and Chemical Engineering, Xiamen University, Xiamen 361005, Fujian, China

<sup>b</sup>National High Magnetic Field Laboratory, 1800 E. Paul Dirac Drive, Tallahassee, FL 32310, USA

## ARTICLE INFO

### Article history:

Received 22 November 2022

Revised 16 June 2023

Accepted 19 June 2023

Available online 20 June 2023

### Keywords:

Sodium-ion batteries

Solid-state NMR

In-situ NMR

Electrode

Interface

## ABSTRACT

In order to develop new electrode and electrolyte materials for advanced sodium-ion batteries (SIBs), it is crucial to understand a number of fundamental issues. These include the compositions of the bulk and interface, the structures of the materials used, and the electrochemical reactions in the batteries. Solid-state NMR (SS-NMR) has unique advantages in characterizing the local or microstructure of solid electrode/electrolyte materials and their interfaces—one such advantage is that these are determined in a noninvasive and nondestructive manner at the atomic level. In this review, we provide a survey of the recent advances in the understanding of the fundamental issues of SIBs using advanced NMR techniques. First, we summarize the applications of SS-NMR in characterizing electrode material structures and solid electrolyte interfaces (SEI). In particular, we elucidate the key role of in-situ NMR/MRI in revealing the complex reactions and degradation mechanisms of SIBs. Next, the characteristics and shortcomings of SS-NMR and MRI techniques in SIBs are also discussed in comparison to similar Li-ion batteries. Finally, an overview of SS-NMR and MRI techniques for sodium batteries are briefly discussed and presented.

© 2023 Elsevier Inc. All rights reserved.

## 1. Introduction

With the increasing demand for large-scale energy storage systems (ESS) for renewable energy applications, sodium-ion batteries (SIBs) have received extensive attention in recent years because of the high natural abundance of sodium. SIBs have a comparable ion transport mechanism and working principle with lithium-ion batteries (LIBs) in the framework of the electrode materials because Na<sup>+</sup> and Li<sup>+</sup> have similar chemical and physical properties.[1–4] However, due to the intrinsic differences between Na<sup>+</sup> and Li<sup>+</sup>, such as ion radius, molar mass, redox potential, solvated structure, and so on, SIBs have shown different chemical/electrochemical behaviors during the material synthesis and battery operations.[5] It would seem that comprehensive and systematic characterization of electrode materials, complex reaction mechanisms, and multiple phase transition processes will be helpful to the rapid development of SIBs with high capacity, high cycling performance, long life, and high safety.

Up until now, quite a few spectroscopic characterization techniques for solid-state materials have been widely utilized in the structural and composition characterization of electrode/electrolyte materials for SIBs.[6] Among them, the X-ray diffraction

(XRD) technique is very successful and mainly used to study the long-range structure of crystalline materials; however, it is not easy to precisely determine the occupancy information of Na<sup>+</sup> in solid materials based on refinement techniques only. X-ray absorption spectroscopy (XAS), Atomic pair distribution function (PDF), and solid-state nuclear magnetic resonance (SS-NMR) are all applied to determine the short-range and local structure of the solid materials in non-crystalline or nanostructured materials. Compared with other spectroscopic characterization techniques, SS-NMR is a powerful tool for non-destructive, quantitative analysis without harsh experimental conditions, such as PDF with its expensive synchrotron radiation sources. As for composition characterization, X-ray photoelectron spectroscopy (XPS) has been widely applied in surface analysis of materials; however, the quantitative peak fitting and assignment of XPS is difficult, although may be improved by computational methods.[7,8] By contrast, SS-NMR can directly provide valid information not only on the local structure of the targeted nuclei but also on the ionic diffusion and reaction processes, such as Li/Na deposition-stripping at solid–solid or solid–liquid interfaces.[9] NMR spectra of the charge carriers and lattice framework elements (<sup>7</sup>Li, <sup>6</sup>Li, <sup>23</sup>Na, <sup>31</sup>P, <sup>11</sup>B, <sup>19</sup>F, <sup>51</sup>V, etc.) in SIBs[10,11] can not only disclose the compositions and structures of electrode or interface, but also provide unique advantages in the characterization of amorphous solid materials—such as

\* Corresponding author.

E-mail address: [yyang@xmu.edu.cn](mailto:yyang@xmu.edu.cn) (Y. Yang).

hard carbon and alloy electrodes—which cannot be analyzed by routine XRD. In addition, magnetic resonance imaging (MRI) can be extended to non-invasive and in-situ electrochemical study and thus is capable of disclosing the mechanism of  $\text{Na}^+$  diffusion and electrode/electrolyte interface evolution in space and time.

Different from liquid samples, solid samples exhibit highly restricted ionic motion resulting in broad resonances in SS-NMR spectra due to the presence of various anisotropic interactions. However, the high-resolution SS-NMR spectra can be effectively achieved by removing those anisotropic interactions through the fast spinning of samples along the axis tilted by  $54.7^\circ$  away from the magnetic field direction, i.e., the so-called magic-angle. Sodium layered oxides and polyanion-type cathode materials of SIBs normally contain 3d/4d transition metal (TM) elements with unpaired electrons (i.e., Mn, Fe-based paramagnetic materials), which lead to the spin density of the unpaired electrons transfer from TM ions to Na nuclei. This interaction significantly broadens  $^{23}\text{Na}$  signals and greatly shifts their chemical shifts, capable of providing abundant information on the framework, microstructure, and chemical environment of cathode materials. Conversely, anode materials are mostly conductors or semiconductors with conductive electrons. Because of the affiliated effect of conductive electrons on the Na spin, the Knight shift of  $^{23}\text{Na}$  in the static magnetic field will significantly affect the chemical shift of sodium metal-based anode materials, so that the different material morphologies and phases can be distinguished. For example, in the  $\text{Na}[\text{Na}_3\text{V}_2(\text{PO}_4)_3]$  cells, the chemical shift of cathode materials is about 20–250 ppm with the different charge or discharge processes, the signals from SEI and electrolyte species appear at around 0 ppm, while the signal of sodium metal resonances appears at around 1130 ppm. Therefore, SS-NMR can effectively distinguish different chemical components in SIBs. For the solid-state electrolytes with low electronic conductance, the NMR signals of solid-state electrolytes are closely related to ionic transport. By using well-designed pulse sequences and with the help of pulse-gradient field, SS-NMR can be applied to characterize the ionic dynamics of solid-state electrolytes such as intrinsic diffusion coefficients at different temperatures. Previous reviews mostly summarized in detail the principles of SS-NMR, in-situ SS-NMR, and their applications in LIBs and SIBs. [10–13] However, there is a lack of timely reviews or perspective papers on SS-NMR techniques that can be applied to SIBs.

In this review, we summarize the recent advances in the applications of NMR techniques in electrodes, electrolytes, and their interfaces in SIBs. We prospect the future applications of the SS-NMR techniques in various materials and operando characterizations of SIBs. It is expected that this article could provide readers with a comprehensive understanding of the unique advantages of SS-NMR in the SIBs characterizations and stimulate new ideas for subsequent research.

## 2. Solid electrode materials

In this section, the applications of SS-NMR in solid-state materials for SIBs, including cathode materials and anode materials (hard carbon, graphite, alloy anode electrodes, etc.) in recent years are summarized. Specifically, we present some examples such as structural characterization, ionic dynamics (Na-ion diffusion), phase transition processes during charge–discharge cycling, and the intercalation/deintercalation mechanism of  $\text{Na}^+$  in electrode materials.

### 2.1. Cathode materials

At present, the cathode materials applied in SIBs mainly include sodium-based layered oxides, polyanion materials, Prus-

sian blue analogs, etc. The unpaired 3d electrons of TMs used in the sodium cathode materials (Mn, Fe, V, etc.) make these cathodes paramagnetic and result in hyperfine interactions between Tm and  $\text{Na}^+$  ions through the M–O–Na bond. These complex interactions lead to broad  $^{23}\text{Na}$  NMR resonances and expand their chemical shifts. On the other hand, they also provide rich and sensitive structural information about the material lattice framework.

#### 2.1.1. Sodium layered oxides

With the advantages of low cost, easy synthesis, and high specific capacity, sodium layered oxides ( $\text{Na}_x\text{TmO}_2$ , Tm = Mn, Fe, Co, Ni, etc.) are considered as the most-investigated cathode materials for SIBs. Mn is both more environmentally friendly and more abundant in the earth's crust (38.1 folds of Co and 11.3 folds of Ni), plus Mn-based sodium layered oxides also have higher redox potential than the Fe-based sodium layered oxides. Therefore, Mn is attractive as the main TMs for low-cost layered cathode materials. However, the Mn-based materials also encounter some problems such as Mn-ions migration and Mn(III)/Mn(IV) Jahn–Teller distortion in O3/P2/P2'– $\text{Na}_x\text{MnO}_2$ , which could result in serious instability of cycling performance and dissolutions of Mn-ions in the electrolytes.

SS-NMR has been widely applied to characterize the local structural evolutions and corresponding localized phase transition processes of the electrode materials after different ionic doping. As early as 2014, Grey et al. first investigated the signal peak changes of  $\text{Na}_x\text{MnO}_2$  ( $x = 1.0\text{--}0.24\text{--}0.92$ ) during the first cycle via  $^{23}\text{Na}$  magic-angle spinning (MAS) SS-NMR [14] and then proposed the function of Mg ions on the Mg-doped  $\text{Na}_x\text{Mn}_{1-y}\text{Mg}_y\text{O}_2$  ( $y = 0.05$ ). [15] In recent years, there was more research focused on the P2– $\text{Na}_{0.67}\text{MnO}_2$ , suggesting that expanding the interspacing of the Na-layer could be beneficial for  $\text{Na}^+$  diffusion as well as suppressing the Tm–O layer phase transition process (Fig. 1a). [16] Zuo et al. successfully expanded the  $\text{Na}^+$  layer of P2– $\text{Na}_{0.67}\text{MnO}_2$  by using the water-mediated method (S-NMO). [17] As shown in Fig. 1b, the ex-situ  $^{23}\text{Na}$  MAS NMR signals of S-NMO located at 0, 200–500, 800–900, 900–1450, and 1700–1900 ppm, correspond to the diamagnetic sodium salt, hydration, P2' phase ( $\text{Mn}^{3+}$ -rich), P2 phase and the  $\text{Mn}^{4+}$ -rich local environment, respectively. During the first discharge process, the  $\text{Mn}^{4+}$ -rich local environment disappeared and the P2' phase appeared. During the second charge process, the P2' phase disappeared and the  $\text{Mn}^{4+}$ -rich local environment recovered at 3.5 V.  $^{23}\text{Na}$  rotational-echo double-resonance (REDOR) MAS NMR spectroscopy [18] indicated that  $\text{NaHCO}_3$  and  $\text{H}_2\text{O}$  impurities had been removed from the S-NMO electrode. Combined with the XRD results, these NMR results suggest that the S-NMO electrode exhibits high structural stability and cycling reversibility. Apart from this work, ion doping or co-doping of various metal ions can also inhibit phase transition and improve structural stability for the layered oxides, such as  $\text{Li}^+$  [19],  $\text{Zn}^{2+}$  [20],  $\text{Fe}^{3+}$  [21],  $\text{Ni}^{2+}$  [22], and so on. It is worth mentioning that the  $^7\text{Li}$  SS-NMR can be applied to characterize the ion transport mechanism and local environment in  $\text{Na}^+$ -layer and TM-layer. Wang et al. designed a dual honeycomb-superlattice structure material,  $\text{Na}_{2/3}[\text{Li}_{1/7}\text{Mn}_{5/14}][\text{Mg}_{1/7}\text{Mn}_{5/14}]\text{O}_2$ . [19] Their  $^7\text{Li}$  MAS SS-NMR indicated that the superstructure transformation takes place during the charge–discharge process. This work demonstrated that the Mg– $\text{Mn}_6$  structure formed by  $\text{Mg}^{2+}$  doping contributes to the reversible migration of  $\text{Li}^+$  between the  $\text{Na}^+$ -layer and TM-layer (Fig. 1c).  $^7\text{Li}$ ,  $^6\text{Li}$ , and  $^{23}\text{Na}$  SS-NMR are important tools to understand the ion sites, transport paths, and local environment of doping ions in Li-containing sodium layered oxides. Currently, the research on other layered oxides, such as P2– $\text{Na}_x\text{CoO}_2$  [23], O3-type  $\text{NaLi}_{1/3}\text{Mn}_{2/3}\text{O}_2$  [24], O'3-layered  $\text{Na}_{3+x}\text{Ni}_{2-2x}\text{Fe}_x\text{SbO}_6$  [25], etc. has started to emerge.

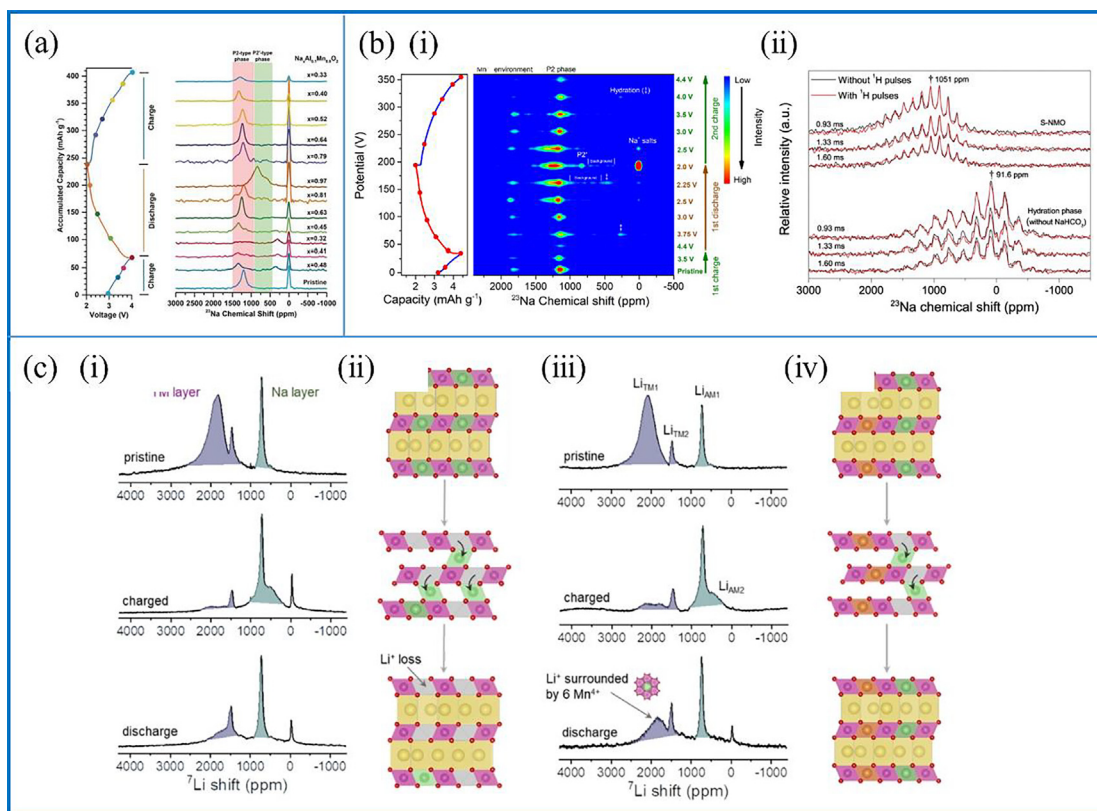


**Fig. 1.** Structural evolution and ion diffusion in Mn-based sodium layered oxides. (a) Ex-situ  $^{23}\text{Na}$  NMR spectra during the initial charge–discharge cycles of  $\text{Na}_{0.67}\text{Al}_{0.1}\text{Mn}_{0.9}\text{O}_2$ . Reproduced with permission from [16]. (b) (i) Ex-situ  $^{23}\text{Na}$  NMR spectra of S-NMO during the charge–discharge processes. (ii)  $^{23}\text{Na}$  REDOR-dephased MAS NMR spectra of S-NMO and hydration phase. Reproduced with permission from [17]. (c) (i)  $^7\text{Li}$  NMR spectra of (i)  $\text{LiMn}_6$  and (ii)  $\text{LiMn}_6\text{-MgMn}_6$  and the layer stacking schematic of (ii)  $\text{LiMn}_6$  and (iv)  $\text{LiMn}_6\text{-MgMn}_6$  which displays chiefly reversible  $\text{Li}^+$  migration at different stages of the first cycle. Reproduced with permission from [19].

### 2.1.2. Polyanion materials

Polyanion materials have high structural stability, safety, and operating voltage, which have received wide attention. However, these materials have intrinsic problems with low electron conductivity and volumetric energy density. Commonly used anions include  $\text{PO}_4^{3-}$ ,  $\text{P}_2\text{O}_7^{4-}$ ,  $\text{SO}_4^{2-}$ ,  $\text{SiO}_4^{2-}$  and  $\text{F}^-$ , while the Tm ions are mainly V, Fe, Mn, etc.[5] Liu et al. employed  $^{23}\text{Na}$  SS-NMR spectroscopy in complementary with XRD to get insights into the mechanism of sodium extraction from  $\text{Na}_3\text{V}_2(\text{PO}_4)_2\text{F}_3$  in SIBs.[26] They found no noticeable preference between Na1 and Na2 removal in Stage I during the charging process. In addition, the broad resonance at 130 ppm corresponding to  $\text{Na}_{2.1}\text{V}_2(\text{PO}_4)_2\text{F}_3$  showed the fast Na1–Na2 exchange motion in the electrolytes, which cannot be seen with by XRD techniques (Fig. 2a). Liao et al. observed the local environment of the  $\text{Na}^+$  in  $\text{Na}_3\text{V}_2(\text{PO}_4)_3$  using  $^{23}\text{Na}$  SS-NMR.[27] As shown in Fig. 2a, the  $^{23}\text{Na}$  MAS SS-NMR and spin–spin relaxation time ( $T_2$ ) measurements assigned the two types of  $\text{Na}^+$  (M1–6b sites and M2–18e sites) in  $\text{Na}_3\text{V}_2(\text{PO}_4)_3$ , which correspond to the (R3c) space group. The signals at  $\sim 80$  and  $\sim 16$  ppm were respectively attributed to the M2– $\text{Na}^+$  and M1– $\text{Na}^+$ . A newly merged signal at  $\sim 223$  ppm after the first charge process to 4.3 V (corresponding to the local environment of  $\text{V}^{4+}$ ) and a new resonance at  $\sim 137$  ppm after the first discharge process to 1.0 V (corresponding to the local environment of  $\text{V}^{2+}$ ) had been found (Fig. 2b). These  $^{23}\text{Na}$  MAS SS-NMR results suggest that the structural formations are highly reversible during the charge–discharge processes.

Furthermore, ion doping strategies can also be applied to improve the structural stability and operating voltage of polyanion materials. Ghosh et al. explored the  $\text{Mg}^{2+}$  doped NASICON- $\text{Na}_{3+y}\text{V}_{2-y}\text{Mg}_y(\text{PO}_4)_3$  cathodes.[28] Doping of diamagnetic  $\text{Mg}^{2+}$  reduced

the hyperfine interactions and thus led to a decrease in linewidths for the  $^{23}\text{Na}$  and  $^{31}\text{P}$  resonances.  $^{23}\text{Na}$  and  $^{31}\text{P}$  SS-NMR proved the non-linear changes in the  $\text{Na}^+$  diffusion properties with the different amounts of  $\text{Mg}^{2+}$  (Fig. 2c). However, the coalescence of Na (1) and Na (2) due to their fast chemical exchange makes it difficult to characterize the complex local environment of individual  $\text{Na}^+$  after random doping of  $\text{Mg}^{2+}$ . In addition,  $^{23}\text{Na}$  SS-NMR can also be applied in the phase identification of new materials, structure evolution, and reaction mechanisms. Nowadays, other polyanion materials, such as  $\text{Na}_3\text{V}(\text{PO}_4)_2$ [29],  $\text{NaVOPO}_4$ [30],  $\text{Na}_4\text{FeV}(\text{PO}_4)_3$ [31],  $\text{Na}_2\text{Mn}_{3-x}\text{Al}_x(\text{VO}_4)_3$ [32],  $\text{Na}_{2.4}\text{Li}_{0.6}\text{V}_2(\text{PO}_4)_2\text{F}_{2.5}\text{O}_{0.5}$ [33] have been studied and characterized.  $^{51}\text{V}$ [30] and  $^{27}\text{Al}$ [32] have also been applied to determine the local environment and structure. In addition, due to the sensitivity of SS-NMR to the local chemical environment, SS-NMR spectroscopy of other metal ions can greatly further understand the framework structure of polyanion materials.

### 2.1.3. Conversion-type cathode materials

Apart from the layered oxides and polyanion materials, several cathode materials have been suggested and analyzed via SS-NMR. As one of the low-cost and earth-abundant species,  $\text{Na}_3\text{FeF}_6$  displayed an initial reversible capacity of  $140 \text{ mA h g}^{-1}$ . Foley et al. identified that  $\text{Na}_3\text{FeF}_6$  was partly converted to  $\text{NaF}$  and  $\text{Fe}$  during the discharging process via the quantitative analysis of the formed  $\text{NaF}$  and  $\text{Fe}$  by  $^{23}\text{Na}$  SS-NMR and  $^{57}\text{Fe}$  Mössbauer spectroscopy first. [34] In addition, SS-NMR had been applied in several cathode materials, such as fluorinated carbon fiber ( $\text{CF}_{0.75}$ )[35], organic cathode material (tetrakislawsonite (TKL))[36], etc. The application of  $^{13}\text{C}$  cross-polarization (CP)–MAS NMR in TKL provides a powerful

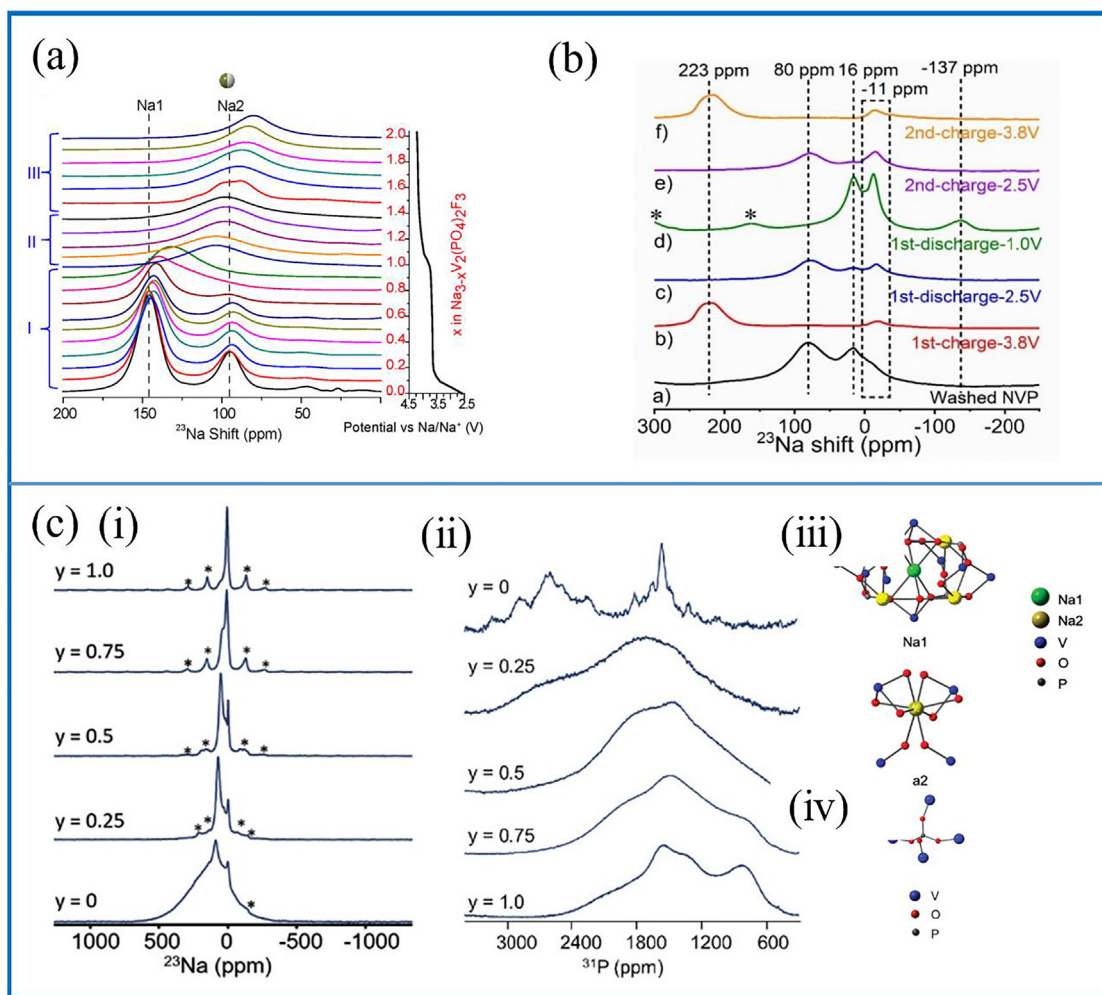


**Fig. 2.** Local structures and  $\text{Na}^+$  sites in polyanion materials. (a) Ex-situ  $^{23}\text{Na}$  NMR spectra of  $\text{Na}_3\text{V}_2(\text{PO}_4)_2\text{F}_3$  electrodes at different states of charge. Reproduced with permission from [26]. (b)  $^{23}\text{Na}$  SS-NMR spectra of  $\text{Na}_3\text{V}_2(\text{PO}_4)_3$  at different charge-discharge processes at 30 kHz MAS and 278 K. Reproduced with permission from [27]. (c) (i)  $^{23}\text{Na}$  and (ii)  $^{31}\text{P}$  SS-NMR spectra of NASICON- $\text{Na}_{3+y}\text{V}_{2-y}\text{Mg}_y(\text{PO}_4)_3$  ( $y = 0, 0.25, 0.5, 0.75, 1.0$ ) cathodes and the (iii) Na or (iv) P local environment in  $\text{Na}_3\text{V}_2(\text{PO}_4)_3$ . Reproduced with permission from [28].

tool to analyze the rare nuclei of organic cathode materials or other carbonaceous electrode materials with high precision.

More research on SS-NMR techniques in cathode material characterizations for SIBs are summarized in Table 1.

## 2.2. Anode materials

Unlike LIBs, commercial graphite anodes are not suitable for SIBs, because  $\text{Na}^+$  cannot be directly intercalated into the graphite layer. Instead,  $\text{Na}^+$  can only be co-intercalated with the ether-based electrolyte. Among the low-cost carbon anodes, hard carbon has attracted more attention in SIBs since 1990[46] with its high energy density and structural stability. However, the mechanism of  $\text{Na}^+$  diffusion in hard carbon is not fully studied. Furthermore, sodium metal anodes (SMAs), alloy anodes, and phosphorus anodes have also been reported.

SS-NMR has outstanding advantages in characterizing amorphous materials. In this section, we will summarize the applications of SS-NMR in these anode materials, especially the  $\text{Na}^+$  diffusion mechanism, sodium deposition, and alloying process.

### 2.2.1. Hard carbon

Hard carbon is a class of non-graphitizing, long-range random disordered, short-range graphite-like stacking ordered carbon

materials, which contains multiple types of  $\text{Na}^+$  storage sites including the filling of graphite layers/pores and the adsorption at defects. The ‘house of cards’ structure is the most widely accepted structural model.[47] Due to the complex structure, the theoretical capacity of hard carbon remains undetermined. Therefore, the development of hard carbon anodes with good electrochemical cycling performance requires a more in-depth understanding and analysis of the structure and  $\text{Na}^+$  storage mechanism by SS-NMR[48], wide-angle X-ray scattering (WAXS)[49], galvanostatic intermittent titration technique (GITT)[50], etc.

$^{23}\text{Na}$  SS-NMR had been applied to analyze the synthesis temperatures[51], charging-discharging curves under 0.1 V[52], quasi-metallic sodium cluster[53], and electrolyte additive (FEC)[54] of the hard carbon; work that has been summarized in detail before [11]. In recent years, Au et al. proposed the direct relationship between the increasing metallic sodium clusters and the growing pore size in the samples which exhibited a low voltage plateau via ex-situ  $^{23}\text{Na}$  SS-NMR (Fig. 3a)[48]. Kim et al. observed the microcrystalline cellulose (MCC)-based hard carbon without any amorphous grains.[55] Compared with the fiber cellulose (FC)-based hard carbon,  $^{23}\text{Na}$  SS-NMR showed a different signal at 9 ppm in MCC-based hard carbon during the fully sodium intercalated process. This signal suggested a lower electron density of the center sodium than that of the intercalated sodium, such as the

**Table 1**  
SS-NMR techniques in cathode materials for SIBs.

Materials	Contents	SS-NMR Experimental details			Chemical shift	Ref
		Nuclei	MHz	MAS		
<b>Sodium Layer Oxides</b>						
P2-Na <sub>2/3</sub> Mn <sub>1-y</sub> Mg <sub>y</sub> O <sub>2</sub>	Effect of Mg doping on the local structure	<sup>23</sup> Na MAS SS-NMR	200 MHz	60 kHz	1450 and 1100 ppm (Mg doping, P2, and OP4)	[15]
β-NaMnO <sub>2</sub>	Structural evolution	<sup>23</sup> Na MAS SS-NMR	1000 MHz	60 kHz	318 ppm (Na <sub>β</sub> ), 528 ppm (Na <sub>SP</sub> ), 751 ppm (Na <sub>α</sub> )	[37]
P2-Na <sub>0.78</sub> Ni <sub>0.23</sub> Mn <sub>0.69</sub> O <sub>2</sub>	Structural evolution	<sup>23</sup> Na MAS SS-NMR	200 MHz	60 kHz	984 ~ 1423 ppm (P2 phase)	[38]
P2-Na <sub>0.67</sub> Al <sub>x</sub> Mn <sub>1-x</sub> O <sub>2</sub>	Effect of Al doping on the local structure	<sup>23</sup> Na pj-MATPASS SS-NMR	400 MHz	55 kHz	650 ~ 900 ppm (P2' phase), 900 ~ 1400 ppm (P2 phase)	[16]
P2-Na <sub>0.6</sub> [Li <sub>0.2</sub> Mn <sub>0.8</sub> ]O <sub>2</sub>	Li <sup>+</sup> sites and migration between TM and Na layer	<sup>6</sup> Li MAS SS-NMR	400 MHz	19 kHz	~720 ppm (Li <sub>AM</sub> ), ~1800 ppm (Li <sub>TM</sub> )	[39]
P2-Na <sub>0.75</sub> [Li <sub>0.25</sub> Mn <sub>0.75</sub> ]O <sub>2</sub>	Structure and phase changes	<sup>23</sup> Na pj-MATPASS SS-NMR	400 MHz	38 kHz	~600 ppm (Li <sub>AM</sub> ), ~2200 ppm (Li <sub>TM</sub> )	[21]
P2-Na <sub>0.67</sub> Al <sub>0.1</sub> Fe <sub>0.05</sub> Mn <sub>0.85</sub> O <sub>2-LN</sub>	Effect of M-ion doping on the phase				1200 ~ 1450 ppm (P2 phase), ~1100 ppm ("Z" phase), ~850 ppm (P2' phase)	[21]
P2-Na <sub>0.67</sub> M <sub>0.1</sub> Mn <sub>0.9</sub> O <sub>2</sub> (M = Li <sup>+</sup> , Mg <sup>2+</sup> , Al <sup>3+</sup> )	Effect of Zn doping on the local structure	<sup>23</sup> Na MAS SS-NMR	400 MHz	55 kHz	1000 ~ 1500 ppm (P2 phase), 750 ~ 1000 ppm (P2' phase)	[20]
P2-Na <sub>0.67</sub> Zn <sub>0.1</sub> Mn <sub>0.9</sub> O <sub>2</sub>	Effect of Zn doping on the local structure	<sup>23</sup> Na MAS SS-NMR	400 MHz	50 kHz	1000 ~ 1600 ppm (P2 phase)	[20]
O3-NaLi <sub>1/3</sub> Mn <sub>2/3</sub> O <sub>2</sub>	irreversible migration of Li <sup>+</sup> to the Na layers	<sup>23</sup> Na and <sup>7</sup> Li MAS SS-NMR	200 MHz	62.5 kHz	1980 ppm (Na 4 h), 2170 ppm (Na 2c)	[24]
P2-Na <sub>0.67</sub> Mn <sub>0.6</sub> Ni <sub>0.2</sub> Li <sub>0.2</sub> O <sub>2</sub>	Sites of doped Li <sup>+</sup>	<sup>23</sup> Na, <sup>6/7</sup> Li MAS SS-NMR	300 MHz	50 kHz	<sup>23</sup> Na: 1200 ~ 1750 ppm. <sup>6/7</sup> Li: 1750 and 750 ppm (Li <sup>+</sup> in TMO and Na layer, respectively).	[40]
S-NMO	Existence of H <sub>2</sub> O and H <sup>+</sup> in the hydration phase	<sup>23</sup> Na{ <sup>1</sup> H} REDOR MAS NMR	400 MHz	55 kHz	91.6 ppm (hydration phase), 1051 ppm (S-NMO)	[17]
	Structural evolution	<sup>23</sup> Na MAS SS-NMR			200 ~ 500 ppm (hydration phase), 800 ~ 900 ppm (P2' phase), 900 ~ 1450 ppm (P2 phase), 1813 ppm (Mn <sup>4+</sup> -rich)	[23]
P2-Na <sub>x</sub> CoO <sub>2</sub>	local structure and electronic property evolution	<sup>23</sup> Na MAS SS-NMR	300 MHz	30 kHz	200 ~ 400 ppm (P2 phases), 100 ~ 200 ppm ("OP" phase)	[23]
O3-Na <sub>3+x</sub> Ni <sub>2-2x</sub> Fe <sub>x</sub> SbO <sub>6</sub> (0 ≤ x ≤ 0.5)	Sites and pathway of Na <sup>+</sup>	<sup>23</sup> Na pj-MATPASS SS-NMR	400 MHz	13 kHz	1300 ~ 1600 ppm (Na(1) and Na(2) sites), ~300 and ~ 180 ppm (Na(3) site)	[25]
P2-Na <sub>0.75</sub> [Li <sub>0.15</sub> Ni <sub>0.15</sub> Mn <sub>0.7</sub> ]O <sub>2</sub>	Migration of Li between the TM layer and Na layer	<sup>7</sup> Li pj-MATPASS SS-NMR	600 MHz	50 kHz	0 ~ 1100 ppm (Li in Na layers), 1100 ~ 2400 ppm (Li in TM layers)	[41]
P2-Na <sub>2/3</sub> [Li <sub>1/7</sub> Mn <sub>5/14</sub> ][Mg <sub>1/7</sub> Mn <sub>5/14</sub> ]O <sub>2</sub>	Reversible Li <sup>+</sup> migration of LiMn <sub>6</sub> -MgMn <sub>6</sub> states	<sup>7</sup> Li pj-MATPASS SS-NMR	400 MHz	30 kHz	2000 and 1500 ppm (Li <sub>TM1</sub> and Li <sub>TM2</sub> ), ~750 ppm (Li <sub>AM1</sub> and Li <sub>AM2</sub> )	[19]
<b>Polyanion Materials</b>						
Na <sub>3</sub> V <sub>2</sub> (PO <sub>4</sub> ) <sub>2</sub> F <sub>3</sub>	Structural/ dynamical changes and fast Na1-Na2 sites exchange	<sup>23</sup> Na MAS SS-NMR <sup>31</sup> P MAS SS-NMR	700 MHz 200 MHz	50 kHz 40 kHz	146 and 92 ppm (Na1 and Na2 sites) 6096 and 4600 ppm (P1 and P2 sites)	[26]
Na <sub>2</sub> FePO <sub>4</sub> F	Local structure, ion mobility, and exchange	in-situ <sup>23</sup> Na SS-NMR <sup>23</sup> Na MAS and 2D EXSY SS-NMR	300 MHz 300 MHz	— 65 kHz	~160 ppm (Na1 and Na2 sites) -175 and 450 ppm (Na1 and Na2 sites), 320 ppm (NaFePO <sub>4</sub> F)	[42]
Na <sub>3</sub> V <sub>2</sub> (PO <sub>4</sub> ) <sub>2</sub> O <sub>1.6</sub> F <sub>1.4</sub>	The electrochemical activity of V <sup>IV</sup> and V <sup>III</sup> , Na <sup>+</sup> migration mechanism	<sup>23</sup> Na/ <sup>51</sup> V MAS NMR	600 MHz	24 kHz	<sup>23</sup> Na: ~90 ppm (NV <sup>+4</sup> POF), ~90 and 130 ppm (NV <sup>+3.8</sup> POF) <sup>51</sup> V: [-550, -720] ppm (NV <sup>+3.8</sup> POF)	[43]
Na <sub>2</sub> FePO <sub>4</sub> F	Two two-phase reactions and intermediate phase Na <sub>1.5</sub> FePO <sub>4</sub> F	2D <sup>23</sup> Na MQMAS NMR in-situ <sup>23</sup> Na NMR	300 MHz 400 MHz	— 50-	~90 ppm and ~ 170 ppm (NV <sup>+3.8</sup> POF cycling) -180 and 440 ppm (Na2 and Na1 sites in Na <sub>2</sub> FePO <sub>4</sub> F), 615, 320 and -130 ppm (Na1b', Na1a' and Na2' sites in Na <sub>1.5</sub> FePO <sub>4</sub> F), 345 ppm (Na1'' site in NaFePO <sub>4</sub> F)	[44]
NaVOPO <sub>4</sub>	electrochemical mechanism	<sup>23</sup> Na, <sup>31</sup> P, <sup>51</sup> V MAS SS-NMR	400 MHz	50 kHz	<sup>51</sup> V: -658 ppm (V <sup>5+</sup> ) <sup>23</sup> Na: 108 ppm (NaVOPO <sub>4</sub> ) <sup>31</sup> P: ~2300 ppm (NaVOPO <sub>4</sub> )	[30]
Na <sub>3</sub> V(PO <sub>4</sub> ) <sub>2</sub>	Recognition of multi-electron reactions	<sup>51</sup> V MAS SS-NMR	400 MHz	50 kHz	—	[29]
Na <sub>3+y</sub> V <sub>2-y</sub> Mg <sub>y</sub> (PO <sub>4</sub> ) <sub>3</sub>	Evolution of the local structure with Mg doping	<sup>23</sup> Na, <sup>31</sup> P MAS SS-NMR	300 MHz	30 kHz	<sup>23</sup> Na: 134 ppm (Na nuclei in Na(1a), Na(1b) and Na(2c) sites), 55 ppm (Na nuclei in Na(2a) and Na(2b) sites)	[28]
Na <sub>3.41</sub> Fe <sub>0.59</sub> FeV(PO <sub>4</sub> ) <sub>3</sub>	Na sites and extraction mechanism	<sup>23</sup> Na MAS SS-NMR	800 MHz 400 MHz	8 kHz or 10 kHz	<sup>31</sup> P: >~200 ppm (nuclei in the paramagnetic NASICON cathode) — 5 ppm (Na2), -11 ppm (Na1), -29 ppm (Na1')	[45]

(continued on next page)

Table 1 (continued)

Materials	Contents	SS-NMR Experimental details			Chemical shift	Ref
		Nuclei	MHz	MAS		
Na <sub>3</sub> V <sub>2</sub> (PO <sub>4</sub> ) <sub>3</sub>	Local environment evolution of Na <sup>+</sup> Na <sup>+</sup> sites and electrochemical dynamics	<sup>23</sup> Na MAS SS-NMR	400 MHz	30 kHz	80 and 16 ppm (M2 and M1 sites)	[27]
Na <sub>4</sub> FeV(PO <sub>4</sub> ) <sub>3</sub>		<sup>23</sup> Na MAS SS-NMR	400 MHz	10 kHz	1 ppm (Na1), -15 ppm (Na2)	[31]
Na <sub>2</sub> Mn <sub>2.8</sub> Al <sub>0.2</sub> (VO <sub>4</sub> ) <sub>3</sub>	Effect of Al <sup>3+</sup> doping on the local environment of Na <sup>+</sup>	<sup>23</sup> Na MAS SS-NMR <sup>27</sup> Al MAS SS-NMR	300 MHz 500 MHz	60 kHz 30 kHz	~60 ppm (Na1-a), ~-40 ppm (Na1-b), ~-500 ppm (Na2) ~1000 ppm	[32]
<b>Conversion-type Materials</b>						
Na <sub>3</sub> FeF <sub>6</sub>	Conversion reaction mechanism	<sup>23</sup> Na pj-MATPASS SS-NMR and <sup>19</sup> F, <sup>23</sup> Na MAS SS-NMR	300 MHz	60 kHz	<sup>23</sup> Na: ~0 ppm (NaF), 350 and 1750 ppm (Na2 and Na1 sites) <sup>19</sup> F: -224 ppm (NaF)	[34]
CF <sub>0.75</sub>	Conversion reaction mechanism	<sup>19</sup> F, <sup>23</sup> Na MAS SS-NMR	400 MHz	60 kHz	<sup>19</sup> F: -91 ppm (-C-CF <sub>2</sub> -), (PVDF), -114 ppm (-CF <sub>2</sub> ), -163 ppm (intermediate state CF), -178 ppm (-C-C-F), -191 ppm (covalent CF) <sup>23</sup> Na: 6 ppm (NaF)	[35]
TKL	Na <sup>+</sup> coordination mechanism	<sup>13</sup> C MAS SS-NMR <sup>13</sup> C CP-MAS SS-NMR	600 MHz	10 kHz 20 kHz	128 ppm (sp <sup>2</sup> C), 112 ppm (CF <sub>2</sub> ), 85 ppm (CF) 33 ppm (1NaTKL), 170 ~ 176 ppm (3NaTKL)	[36]

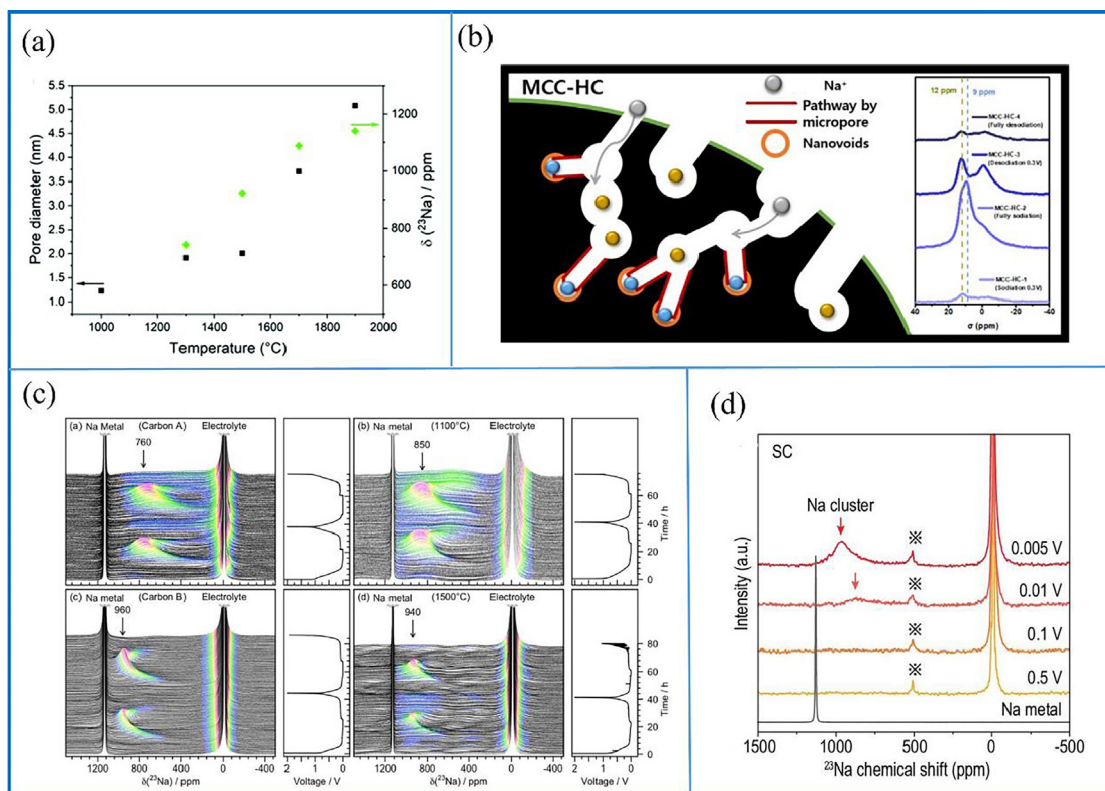


**Fig. 3.** Structure and sodium immobilization mechanism of hard carbon materials. (a) The relationship between the pore diameter, quasi-metallic Na peak shift (based on the ex-situ  $^{23}\text{Na}$  MAS NMR experiments), and sample pyrolysis temperature. Reproduced with permission from [48]. (b) Schematic of  $\text{Na}^+$  insertion mechanism (left) and ex-situ MAS NMR spectra (right) based on the first cycle of MCC-HC. Reproduced with permission from [55]. (c) Operando  $^{23}\text{Na}$  NMR spectra for electrochemical cells with sodium metal and hard carbon electrodes. Reproduced with permission from [56]. (d) Ex-situ  $^{23}\text{Na}$  MAS SS-NMR spectra of SC anodes at various states of charge in the first cycle. Reproduced with permission from [57].

sodium insertion into hard carbon with stacking disorder (Fig. 3b). However, Stratford et al. observed two hard carbon materials with different fragment sizes and  $^{23}\text{Na}$  chemical shifts.[56] The operando  $^{23}\text{Na}$  NMR found that carbon A, which had a smaller fragment size ( $16 \times 17 \text{ \AA}$  vs.  $20 \times 20 \text{ \AA}$  for Carbon B), had a significantly broad  $^{23}\text{Na}$  Knight shift resonance at  $\sim 760$  ppm during the cycling process, indicative of a variety of local sodium environments. Combining with the PDFs, they concluded that the  $^{23}\text{Na}$  NMR Knight shift is not only related to the size of the sodium cluster, but also correlated with the coherence length of the graphene fragments. They also observed that the pore size of hard carbon materials did not necessarily correlate with the size of sodium clusters (Fig. 3c). Recently, Li et al. observed sieving carbons (SCs) as high-energy anodes for SIBs with  $\sim 400$  mAh/g capacity, and the  $^{23}\text{Na}$  SS-NMR resonances at 960 ppm in SCs, arising from the Knight shift, related to the formation of quasi-metallic sodium clusters (Fig. 3d). [57].

Ion doping also significantly affects the properties and sodium storage mechanism of hard carbons. Chen et al. synthesized two types of hard carbons by pyrolysis of glucose (Glu) and MgO-doping glucose (Mg-Glu).[58]  $^{23}\text{Na}$  SS-NMR illuminated the difference in the Knight shift behaviors between Glu and Mg-Glu. During the fully sodium intercalated process, the  $^{23}\text{Na}$  shift of Mg-Glu was larger than that of Glu (1018 ppm vs. 973 ppm), indicating a higher Na 2s state density at the Fermi level. Mg-Glu had a broader and higher chemical shift, associated with the different chemical environments, formation states, and sizes of quasi-metallic sodium clusters (Fig. 4).

In general, the mechanism of sodium storage and diffusion in hard carbons is not yet agreed upon. [59] It seems that SS-NMR will be very helpful to understand the structure-activity relationship of

hard carbons and for optimization of structure design and their electrochemical performance.

## 2.2.2. Graphite-type materials

Although graphite cannot be directly applied to SIBs, Na intercalates with ether-based electrolytes in graphite provide a new idea for the fast-charging capability of SIBs. In previous work, the  $^2\text{H}$  NMR results showed that the diglyme molecules coordinated to the  $\text{Na}^+$  ( $\text{C}_{22-26}(\text{diglyme})_{1.8-2.2}\text{Na}_{1.0}$ ) in sodium-diglyme-graphite structure at low temperature (below 233 K). At room temperature,  $\text{Na}^+$ -diglyme rotated around the Na-O axis, facilitating the rapid  $\text{Na}^+$  diffusion into/out of the graphite.[60] Leifer et al. compared  $\text{Li}^+$ -(diglyme)<sub>2</sub> and  $\text{Na}^+$ -(diglyme)<sub>2</sub> via  $^2\text{H}$  NMR and  $^1\text{H}$ - $^{13}\text{C}$  CP MAS NMR and observed notable free local behavior of  $\text{Na}^+$ -(diglyme)<sub>2</sub> as well as a weak complex between the  $\text{Na}^+$ -(diglyme)<sub>2</sub> and graphene sheets, resulting in the fast diffusion of  $\text{Na}^+$  into graphite.[61] Moreover, the solvent effects had been studied as well.[62,63] But due to the low specific capacity (90–100 mAh/g), research on graphite-type materials has gradually decreased.

## 2.2.3. Sodium metal anodes

Compared with the other anodes, sodium metal anodes have a higher theoretical specific capacity (1167 mAh/g) and lower redox potential (-2.71 V). Unfortunately, due to the uncontrollable interface-side reactions, dendrite growth, and huge volume change, it is difficult for sodium metal anodes to achieve commercial application at the present stage. Thus, non-destructive, in-situ, and quantitative characterization of sodium metal anodes are essential for practical applications.

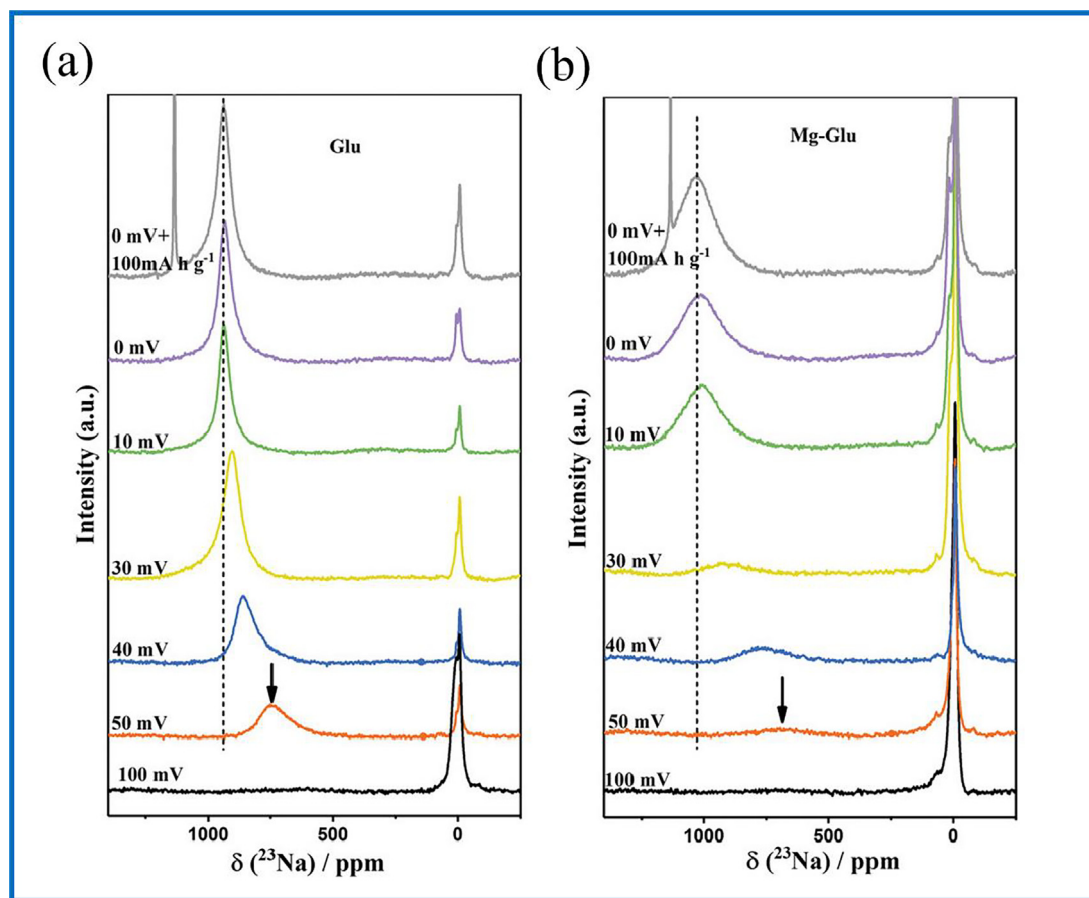


Fig. 4. Ex situ  $^{23}\text{Na}$  MAS NMR spectra of (a) Glu and (b) Mg-Glu at different discharge states. . Reproduced with permission from [58]

SS-NMR has unique advantages for characterizing the microstructure of sodium deposition and detecting the chemical composition of the electrode surface in sodium metal anodes. Bayley et al. applied in-situ SS-NMR to explore the sodium metal anodes for the first time (Fig. 5a). [64] Because the deposited microstructures with high-surface area (HSA) were typically much smaller than the skin depth, they were penetrated fully by radio frequency (RF). In-situ  $^{23}\text{Na}$  SS-NMR results suggested that HSA microstructures were accumulated at all current densities in this study (0.5, 1.0, 2.0  $\text{mA cm}^{-2}$ ). However, with the quantitative analysis of the efficiency in the removal of the HSA microstructures, the nucleation mechanism of lower current density (0.5  $\text{mA cm}^{-2}$ ) and higher current densities (1.0, 2.0  $\text{mA cm}^{-2}$ ) was shown to be quite different. Xiang et al. provided information about the spatial distribution and morphological evolution process of sodium metal microstructures (SMSs) via in-situ  $^{23}\text{Na}$  MRI and observed the mathematical understanding of the correlation of the deposition over-potential and SMSs.[65] As shown in Fig. 5b, the signal in the F2 electrolyte (1 M  $\text{NaClO}_4/\text{PC} + 2 \text{ vol}\% \text{ FEC}$ ) at 1125 ppm had the smooth deposition of sodium metal during cycling, which was consistent with the  $^{23}\text{Na}$  MRI. In the F0 electrolyte (1 M  $\text{NaClO}_4/\text{PC}$ ), the signal at 1100–1200 ppm was gradually increased with long-time cycling, indicating the continuous growth of SMSs. This work provided in-situ and quantitative information on the deposition and stripping behavior of metal anodes with high space–time resolution. In addition, other work focuses on the qualitative and quantitative analysis of the species at the electrode surface, such as SEI, and we will summarize these in detail in Section 3.2.

#### 2.2.4. Alloy anodes

Most alloy anode materials provide higher specific capacity due to the abundant valence changes during the cycling process, but the large volume change restricts its commercial application. In the process of forming alloys between Na and Sn, Sb, P, etc., there will be a large number of amorphous intermediates, which are difficult to characterize by XRD. Combined with the PDFs and calculations, SS-NMR is often used to characterize the intermediate structures and speculate on the mechanism of sodium formation.

Grey et al. first studied the alloying mechanism of Sn and Sb anodes by SS-NMR and PDFs. As for the Sb anode,  $\text{Na}_x\text{Sb}$  at different stages of alloying (different  $x$  values) exhibited different chemical shifts in  $^{23}\text{Na}$  SS-NMR.[66] During the sodiation process, a broad peak at  $\sim 37$  ppm was observed ( $x > 1$ , S1-a as shown in Fig. 6), proving the independent phase of  $\text{NaSb}$  and  $\text{Na}_3\text{Sb}$ , which disappeared in the de-sodiation state. In the second-half state of S1-a, the signal peak at 37 ppm increased and moved to 42 ppm, and an extra signal peak at 50–80 ppm was found, indicating the mixture of several  $\text{Na}_x\text{Sb}$  phases. Combined with the operando PDFs, amorphous  $\text{a-Na}_{1.7}\text{Sb}$ ,  $\text{a-Na}_{3-x}\text{Sb}$  ( $0.4 < x < 0.5$ ) were observed and the different mechanisms of the first sodiation and de-sodiation processes and the second sodiation process proposed (Fig. 6a). Sn electrode has a more complex sodiation mechanism. Based on the previous work,  $\text{Na}_{15+x}\text{Sn}_4$  was considered the final product after the charging process by  $^{119}\text{Sn}$  SS-NMR.[67] Sn-sodiation had five processes (0, 1, 2, 3, 4). Process 0 corresponded with the formation of SEI and the conversion of  $\text{SnO}_2$  or  $\text{SnO}$  to Sn. During process 1, at approximately 450 mV (vs Na metal),  $^{23}\text{Na}$  operando NMR revealed a signal peak with a chemical shift of

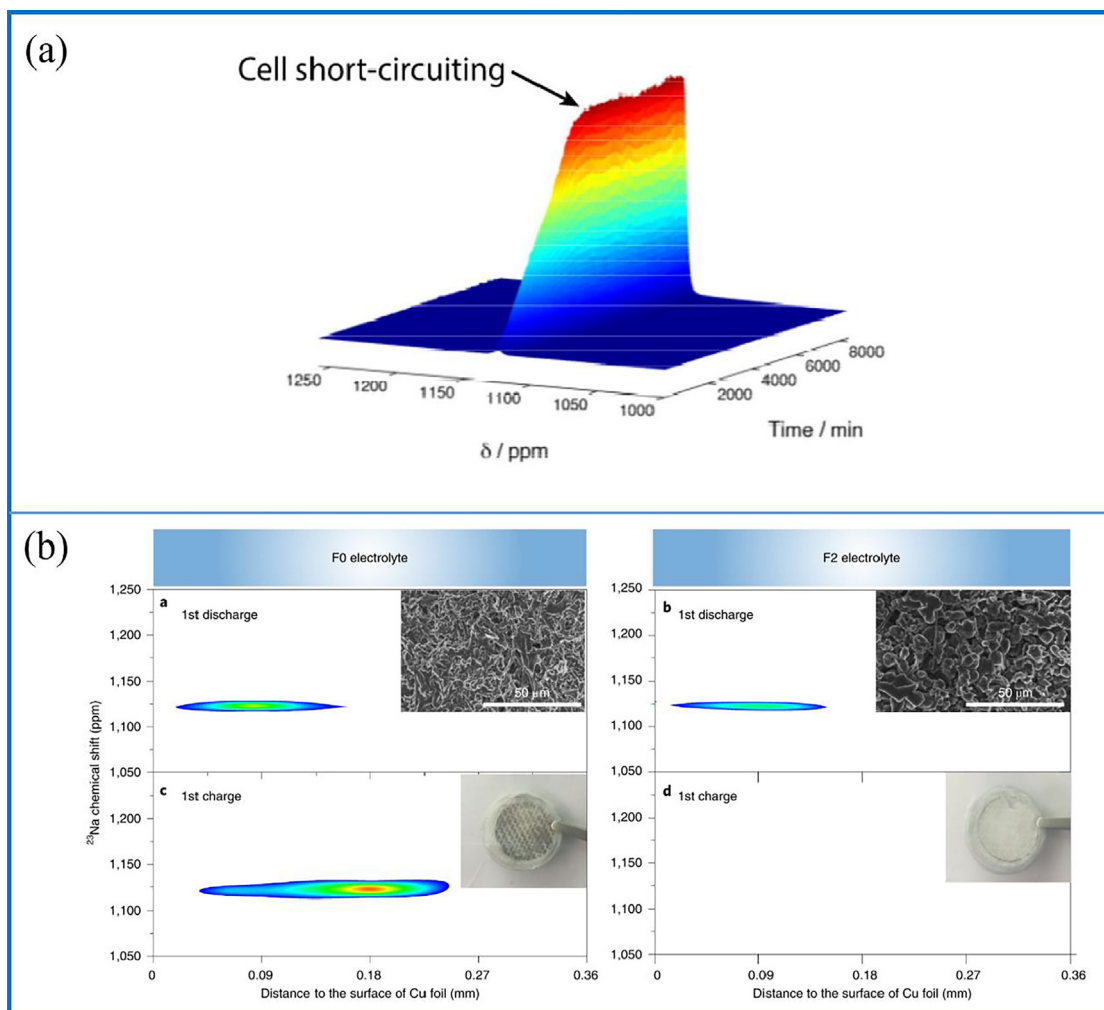


Fig. 5. SS-NMR and MRI study on the sodium metal anode. (a) In-situ  $^{23}\text{Na}$  SS-NMR of sodium deposition. Reproduced with permission from [64]. (b) In-situ  $^{23}\text{Na}$  MRI images of the Na||Cu batteries during the first cycle in F0 (left) and F2 (right) electrolytes. Reproduced with permission from [65].

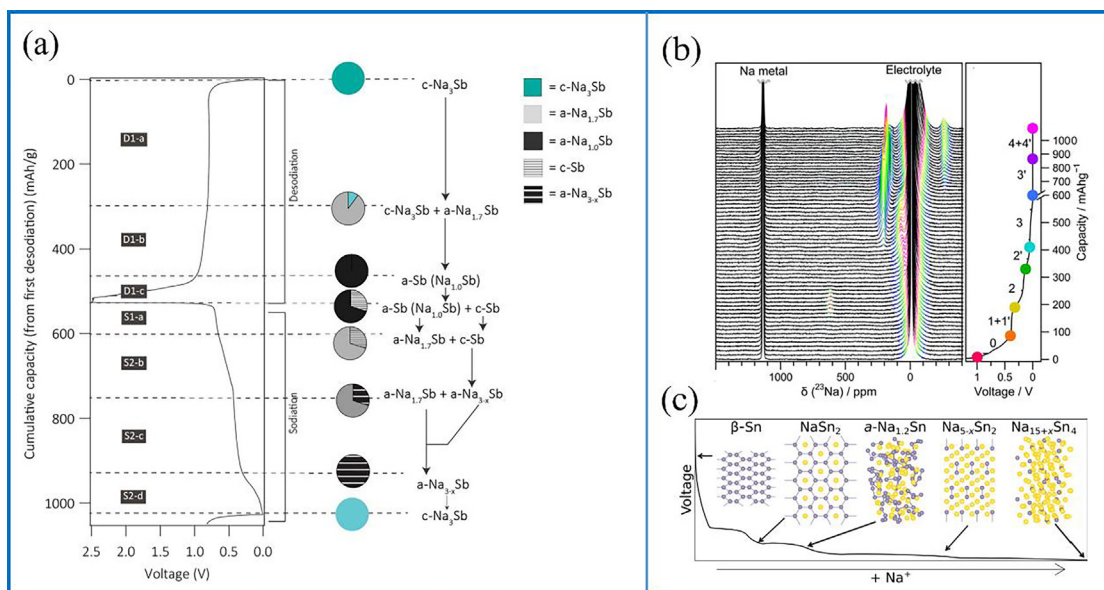
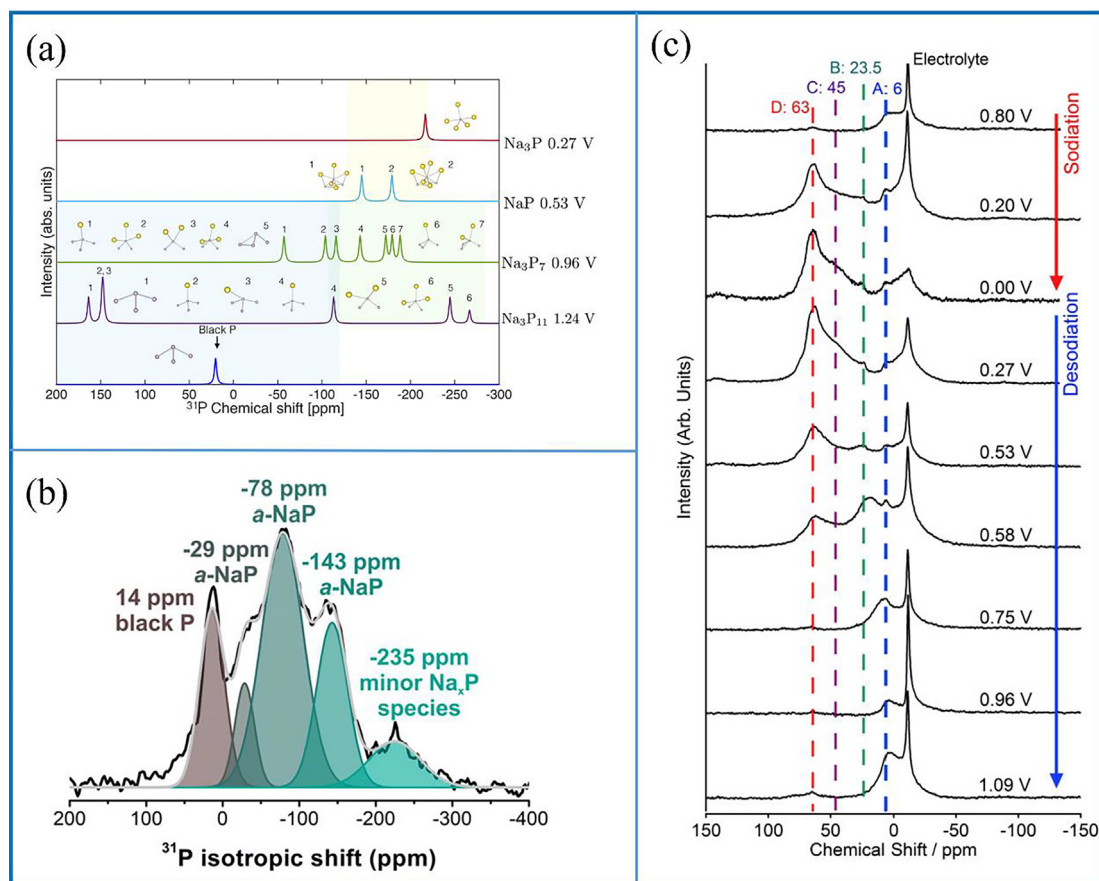


Fig. 6. Alloying reaction mechanism of Sn and Sb. (a) SS-NMR and PDF-derived of (de)sodiation of Sb from the first de-sodiation process during galvanostatic cycling at a rate of 0.05C. Reproduced with permission from [66]. (b) Operando  $^{23}\text{Na}$  NMR spectra were obtained during the first discharge process with the corresponding electrochemistry. Reproduced with permission from [67]. (c) Alloying mechanism and intermediate products of Sn anodes proposed by the NMR, PDF, and XRD characterizations. Reproduced with permission from [67].



**Fig. 7.** Alloying reaction mechanism of P. (a) Calculated  $^{31}\text{P}$  NMR chemical shifts for various Na-P compounds. Reproduced with permission from [68]. (b) Deconvolution of the  $^{31}\text{P}$  isotropic projection from 2D  $^{31}\text{P}$  PASS NMR experiments (black line) performed on a sample of approximate Na-P compositions, extracted from a SIB at 0.38 V ( $780 \text{ mA h g}^{-1}$ ) during sodiation. Reproduced with permission from [69]. (c)  $^{23}\text{Na}$  MAS SS-NMR spectra of electrochemically synthesized Na-P compounds at 10 kHz spinning. Reproduced with permission from [70].

620 ppm, which resembled the  $\text{NaSn}_2$ . During process 2, at approximately 220 mV (vs Na metal), the signal peak at 50–75 ppm corresponded to the a- $\text{Na}_{1.2}\text{Sn}$ . And in the next process, the a- $\text{Na}_{1.2}\text{Sn}$  translated to the  $\text{Na}_{4.4}\text{Sn}$ , with the chemical shift of signal peak turned from 75 to 50 ppm to 202–180 ppm. And in the final process,  $\text{Na}_{15}\text{Sn}_4$  and  $\text{Na}_{15+x}\text{Sn}_4$  were observed with the signal peak at 260 ppm (Fig. 6b). Ex-situ  $^{119}\text{Sn}$  MAS SS-NMR, PDFs, and Ab initio random structure searching (AIRSS) results also confirmed this conclusion (Fig. 6c).

Non-metallic phosphorus anodes (2596 mAh/g) also undergo a similar alloying mechanism during cycling. Mayo et al. predicted the possible alloying mechanism of black phosphorus (BP) and the metastable intermediate and final products during the cycling process ( $\text{Na}_3\text{P}_{11}$ ,  $\text{Na}_3\text{P}_7$ ,  $\text{NaP}$ ,  $\text{Na}_5\text{P}_4$ , and  $\text{Na}_3\text{P}$ ) via calculated  $^{31}\text{P}$  NMR chemical shift and AIRSS (Fig. 7a).[68] Marbella et al. discovered the different mechanisms of BP anode in the first cycling process of sodiation and de-sodiation via ex-situ  $^{31}\text{P}$  MAS NMR. In addition, with the  $^{23}\text{Na}$  SS-NMR and 2D  $^{31}\text{P}$  PASS experiments, a more stable final product c- $\text{Na}_3\text{P}$ - $P6_3cm$  and more amorphous intermediates (a- $\text{Na}_x\text{P}$  with the chemical shift of  $\sim 29$  ppm,  $\sim 78$  ppm, and  $\sim 143$  ppm) were proposed (Fig. 7b).[69] However, Morita et al. observed that the phosphorous anodes exhibited reversible cycling performance at the fourth cycling process, and proposed the occurrence of different chemical shifts during the cycling process using  $^{23}\text{Na}$  and  $^{31}\text{P}$  MAS SS-NMR, as well as  $^{23}\text{Na}$  triple-quantum (3Q) MAS SS-NMR. As shown in Fig. 7c, the signals appeared in different regions, such as  $\text{Na}_{1-\alpha}\text{P}$  (signal A,  $0 < \alpha < 1$ , at 6 ppm of  $^{23}\text{Na}$  NMR and  $\sim 240$  ppm of  $^{31}\text{P}$  NMR),  $\text{Na}_{2-\beta}\text{P}$  (signal B,

$1 < \beta < 2$ , 23.5 ppm of  $^{23}\text{Na}$  NMR and  $\sim 235$  ppm of  $^{31}\text{P}$  NMR),  $\text{Na}_{3-\gamma}\text{P}$  (signal C,  $2 < \gamma < 3$ , 45 ppm of  $^{23}\text{Na}$  NMR and  $\sim 265$  ppm of  $^{31}\text{P}$  NMR) and  $\text{Na}_3\text{P}$  (signal D, 63 ppm of  $^{23}\text{Na}$  NMR and  $\sim 208$  ppm of  $^{31}\text{P}$  NMR).[70] The  $^{31}\text{P}$  signal of  $\text{Na}_3\text{P}$  also appeared in the fully sodiated VP<sub>2</sub> anodes, confirming that the  $\text{Na}_3\text{P}$  was an important final component of sodiation phosphorous anodes. The characterizations of Si-based  $\text{Na}_2\text{SiP}_2$  alloying anodes using  $^{23}\text{Na}$ ,  $^{29}\text{Si}$ , and  $^{29}\text{P}$  SS-NMR are also gradually emerged.[71]

### 2.2.5. Novel anode materials

Ti-based layered materials are potential anode materials for SIBs with good cycling performance and structural stability. Among them,  $\text{Na}_2\text{Ti}_3\text{O}_7$  is the most representative species. Zarrabaitia et al. evaluated the water stability and the spontaneous exchange of  $\text{Na}^+$  by  $\text{H}^+$  of the  $\text{Na}_{2-x}\text{H}_x\text{Ti}_3\text{O}_7$  ( $0 < x < 2$ ) via  $^{23}\text{Na}$  multiple-quantum magic-angle spinning (MQMAS) SS-NMR,  $^{23}\text{Na}$ , and  $^1\text{H}$  MAS SS-NMR.[72] Tsiantsouri et al. reported the exfoliation of  $\text{Na}_2\text{Ti}_3\text{O}_7$  by  $\text{HNO}_3$  and  $\text{NaOH}$  to form  $\text{H}^+$ - $[\text{Ti}_3\text{O}_7]$  and  $\text{Na}^+$ - $[\text{Ti}_3\text{O}_7]$ , confirming the full ion exchange and stable  $[\text{Ti}_3\text{O}_7]^{2-}$  structure via  $^{23}\text{Na}$  and  $^1\text{H}$  MAS SS-NMR.[73] In addition, with the  $^{23}\text{Na}$  MAS SS-NMR, Kajiyama et al. determined the  $\text{Na}^+$  reaction/intercalation mechanism of the MXene ( $\text{M}_{n+1}\text{X}_n\text{T}_x$ ,  $\text{M} = \text{Ti}, \text{V}, \text{Nb}$ , etc.;  $\text{X} = \text{C}, \text{N}$ ;  $\text{N} = 1-3$ ;  $\text{T}_x$  = functional termination group)  $\text{Ti}_3\text{C}_2\text{T}_x$ . [74] Furthermore, SS-NMR has also been applied in the characterization of layered  $\text{CrPS}_4$ [75], organic anodes sodium naphthalene dicarboxylate ( $\text{Na}_2\text{NDC}$ )[76], polymer-derived  $\text{SiCN}$ [77], and  $\text{SiOC}$  [78].

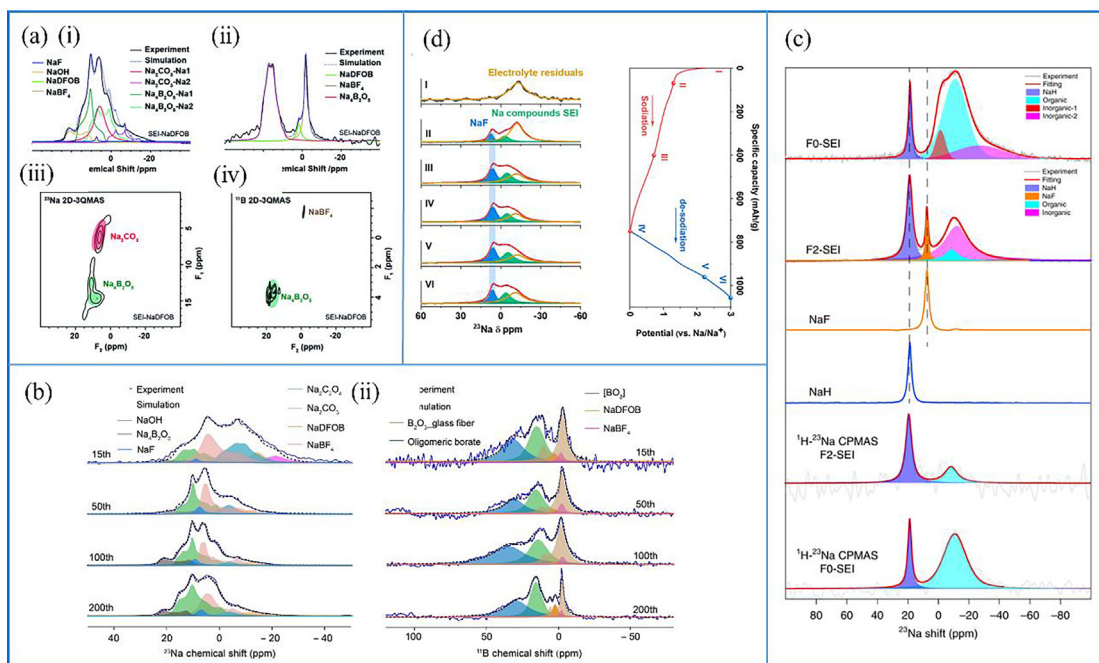
**Table 2**  
SS-NMR techniques in anode materials for SIBs.

Materials	Contents	SS-NMR Experimental details			Chemical shift	Ref
		Nuclei	MHz	MAS		
<b>Hard Carbon</b>						
HC	Sodium storage mechanism	Operando <sup>23</sup> Na SS-NMR and <sup>23</sup> Na MAS SS-NMR (Hahn-echo)	300 MHz 300 MHz	— 60 kHz	−40 ~ 760 ppm (sodiation ≤ 0.8 V) −70 ppm (sodiation 180 mV), 660 ppm (sodiation 5 mV)	[53]
HC (HTC of Glu)	Sodium storage environments	<sup>23</sup> Na MAS SS-NMR	700 MHz	60 kHz	750 ppm (ionic sodium, full sodiation), 1135 ppm (metallic sodium, full sodiation)	[48]
MCC-based HC	Sodium storage behaviors	<sup>23</sup> Na MAS SS-NMR	500 MHz	10 kHz	9 ppm and 12 ppm (intercalated sodium)	[55]
HC (dehydrated Glu)	Local electronic structure	Operando <sup>23</sup> Na SS-NMR	300 MHz	—	760 ~ 960 ppm (ionic sodium, full sodiation)	[56]
HC (Glu and Mg-Glu)	Sodium storage environments	<sup>23</sup> Na MAS SS-NMR	500 MHz	10 kHz	745 ~ 973 ppm (Glu, sodiation), 680 ~ 1018 ppm (Mg-Glu, sodiation)	[59]
HC (sucrose)	Metallic property of sodium clusters (with FEC additive)	<sup>23</sup> Na MAS SS-NMR	500 MHz	10 kHz	800 ~ 1120 ppm (quasi-metallic sodium, full sodiation)	[54]
HC (sucrose)	State of sodium, defect sites in structure.	<sup>23</sup> Na MAS SS-NMR and MQMAS NMR	500 MHz	15 and 20 kHz	−60 ~ 30 ppm (sodiation)	[51]
Sieving carbons	The chemical state of sodium	<sup>23</sup> Na MAS SS-NMR	400 MHz	50 and 55 kHz	960 ~ 1130 ppm (sodium clusters, sodiation)	[58]
Al coat on pre-charged soft carbon	Sodiation mechanism, the composition of surface film	<sup>23</sup> Na MAS SS-NMR (single pulse) <sup>1</sup> H- <sup>13</sup> C CP SS-NMR (INEPT)	200 MHz 200 MHz	10 kHz	−12.2 ppm (intercalated Na), 0 ~ 3 ppm (Na SEI formation), −30 ~ −20 ppm (inserted Na) ~17 ppm (methyl), 70 ~ 72 ppm (ethyl), 159 and 171 ppm (carbonate), 30 ppm (tertiary carbons), ~170 ppm (Na <sub>2</sub> CO <sub>3</sub> ), 120 ppm (bulk carbon)	[79]
<b>Graphite-type Materials</b>						
Na-diglyme-GIC	Dynamics and coordination structure	<sup>2</sup> H and <sup>23</sup> Na MAS SS-NMR	500 MHz	—	<sup>2</sup> H: 167 kHz (−CD <sub>2</sub> −), 50 kHz (−CD <sub>3</sub> ), <sup>23</sup> Na: −50 ~ 10 ppm (Na-diglyme-GIC),	[60]
Graphite	Dynamics of sodium co-intercalation with diglyme	<sup>1</sup> H, <sup>7</sup> Li, <sup>13</sup> C, <sup>23</sup> Na MAS SS-NMR (single pulse), <sup>1</sup> H- <sup>13</sup> C and <sup>1</sup> H- <sup>7</sup> Li CP (INEPT)	200 MHz	8–18 kHz	<sup>1</sup> H: 3.3 ~ 3.5 ppm (liquid diglyme), 3.4 ~ 3.5, and 5.4 ppm (diglyme inside the (t)-GIC galleries). <sup>7</sup> Li: 1.5 ppm (Li <sup>+</sup> co-intercalating with diglyme), 0.5 ppm (uncomplex, intercalated Li <sup>+</sup> ). <sup>13</sup> C: 123, 121, and 89 ppm (graphite), ~120 ppm (aromatic carbons). <sup>23</sup> Na: −12.4 ~ −9.8 ppm (surface film), −8.2 ~ −7.5 ppm (intercalated electrolyte) <sup>1</sup> H- <sup>13</sup> C CP: 71 ppm (diglyme methylene), 60 ppm (methyl), 123 ppm (bulk graphite carbons). <sup>1</sup> H- <sup>13</sup> C INEPT: 58.4 ppm (methyl carbon), ~70.2 and ~ 71.6 ppm (methylene carbons). <sup>1</sup> H- <sup>7</sup> Li CP: 1.5 ppm (diglyme-complexed Li).	[61]
<b>Sodium Metal Anodes</b>						
Sodium metal	microstructures and high-surface-area	In-situ <sup>23</sup> Na SS-NMR	300 MHz	—	~1130 ppm (Na metal)	[64]
Sodium metal	The growth process of SMSs	In-situ <sup>23</sup> Na MRI Operando <sup>23</sup> Na NMR <sup>23</sup> Na MAS SS-NMR (single pulse) <sup>1</sup> H → <sup>23</sup> Na CPMAS NMR	400 MHz — 25 kHz	— — 25 kHz	~1130 ppm (Na metal) 7.2 ppm (NaF), 18.8 ppm (NaH), −11.0 ppm (Na in organic and inorganic species)	[65]
<b>Alloy Anodes</b>						
Sb	Sodium local environments	<sup>23</sup> Na MAS SS-NMR	700 MHz	5 and 10 kHz	~27 and ~ 37 ppm (Na <sub>x</sub> Sb), 50 ~ 80 ppm (Na <sub>3</sub> Sb)	[66]
Sn	Alloying mechanism	Operando <sup>23</sup> Na SS-NMR <sup>23</sup> Na and <sup>119</sup> Sn MAS SS-NMR (Hahn-echo)	300 MHz 200 MHz	— 60 kHz	~620 ppm (NaSn <sub>2</sub> ), 45 ~ 70 ppm (amorphous NaSn), 183 ~ 203 ppm (Na <sub>4</sub> Sn-Na <sub>4.75</sub> Sn <sub>2</sub> ), −75 and −260 ppm (Na <sub>15</sub> Sn <sub>4</sub> and Na <sub>15+x</sub> Sn <sub>4</sub> ) <sup>23</sup> Na: ~420 and 610 ppm (NaSn <sub>2</sub> ), ~19 and 70 ppm (amorphous NaSn) <sup>119</sup> Sn: 6600 and 6275 ppm (NaSn <sub>2</sub> ), 122 and 385 ppm (Na <sub>15</sub> Sn <sub>4</sub> and an additional structurally related phase).	[67]
Black P	Sodiation and desodiation mechanism	<sup>23</sup> Na MAS SS-NMR <sup>31</sup> P MAS SS-NMR (Hahn-echo)	300 and 700 MHz 300 MHz	60 kHz 60 kHz	<sup>23</sup> Na: 69 ~ 93 ppm (Na <sub>3</sub> P-P6 <sub>3</sub> cm) <sup>31</sup> P: 14 ppm (black P), −207 ppm (c-Na <sub>3</sub> P).	[69]
Black P	Sodiation and desodiation mechanism	<sup>23</sup> Na and <sup>31</sup> P MAS SS-NMR <sup>23</sup> Na MQMAS NMR	500 MHz 500 MHz	1, 10, and 13 kHz 20 kHz	<sup>23</sup> Na: 6 ppm (Na <sub>1-β</sub> P), 23.5 ppm (Na <sub>2-β</sub> P), 45 ppm (Na <sub>3-γ</sub> P), 63 ppm (Na <sub>3</sub> P) <sup>31</sup> P: −240 ppm (Na <sub>1-β</sub> P), −235 ppm (Na <sub>2-β</sub> P), −265 ppm (Na <sub>3-γ</sub> P), −208 ppm (Na <sub>3</sub> P) Isotropic spectra: 78.3 and 119.1 ppm (Na <sub>3</sub> P), 18.0 and 22.1 ppm (NaP)	[70]

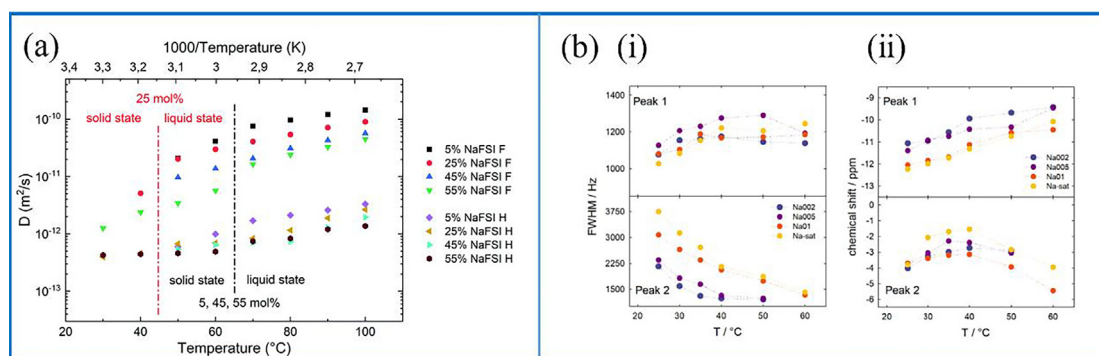
(continued on next page)

Table 2 (continued)

Materials	Contents	SS-NMR Experimental details		Chemical shift	Ref
		Nuclei	MHz MAS		
SiP <sub>2</sub>	Sodiation and desodiation mechanism	<sup>31</sup> P, <sup>23</sup> Na and <sup>19</sup> F MAS SS-NMR	500 MHz 25 and 30 kHz	<sup>31</sup> P: -146 ppm (PF <sub>6</sub> ), 6 ppm (Na <sub>2</sub> HPO <sub>4</sub> ), 13 ppm (Na <sub>3</sub> PO <sub>4</sub> ), 6 ~ 13 ppm (surface P), -100 ppm (bulk SiP <sub>2</sub> ), -235 ppm (sodium-rich phase). <sup>23</sup> Na: -4 ~ 0 ppm (Na in the species formed upon reduction of SiP <sub>2</sub> ), -8.5 ppm (Na ions) <sup>19</sup> F: -225 ppm (NaF), -72 ppm (PF <sub>6</sub> )	[80]
Na <sub>2</sub> SiP <sub>2</sub>	Chemical environments of elements	<sup>23</sup> Na, <sup>29</sup> Si, and <sup>31</sup> P MAS SS-NMR	500 MHz 10 kHz	<sup>31</sup> P: -34.8, -52.6--71.4, and -74.7 ppm (Na <sub>2</sub> SiP <sub>2</sub> ) <sup>29</sup> Si: -35.5, -39.3 and -59.0 ppm (Na <sub>2</sub> SiP <sub>2</sub> ) <sup>23</sup> Na: 8.1 ppm (Na <sub>2</sub> SiP <sub>2</sub> )	[71]
VP <sub>2</sub>	Partial conversion mechanism	<sup>31</sup> P MAS SS-NMR	500 MHz 10 and 12 kHz	300 ~ 900 ppm (VP <sub>2</sub> ), -208.7 ppm (Na <sub>3</sub> P).	[81]
<b>Novel Materials</b> MXene Ti <sub>3</sub> C <sub>2</sub> T <sub>x</sub>	Na <sup>+</sup> intercalation/deintercalation mechanism	<sup>23</sup> Na MAS SS-NMR	500 MHz 18 kHz	-8 and + 5 ppm (Na <sup>+</sup> intercalation/deintercalation)	[74]
CrPS <sub>4</sub>	Sodiation mechanism	<sup>23</sup> Na and <sup>31</sup> P MAS SS-NMR	200 MHz 60 kHz	<sup>23</sup> Na: -100~+200 ppm (sodiation), 49.6 and 6.9 ppm (Na <sub>2</sub> S and NaF) <sup>31</sup> P: -100~+200 ppm (+2Na), 39.4 and 15.2 ppm (+4Na), ~89.4 ppm (+5Na).	[75]
Na <sub>2-x</sub> H <sub>x</sub> Ti <sub>3</sub> O <sub>7</sub>	Spontaneous Na <sup>+</sup> /H <sup>+</sup> exchange	<sup>23</sup> Na and <sup>1</sup> H MAS SS-NMR, <sup>23</sup> Na MQMAS SS-NMR	500 MHz 20 kHz	<sup>1</sup> H: 4.5 ppm (H <sub>2</sub> O), 11.5 ppm (Na <sub>2-x</sub> H <sub>x</sub> Ti <sub>3</sub> O <sub>7</sub> -H <sub>2</sub> O). <sup>23</sup> Na: -100 ~ 20 ppm (NHTO <sub>7</sub> -H <sub>2</sub> O), -60 ~ 20 ppm (NHTO <sub>7</sub> -HCl)	[72]
Na <sub>2</sub> Ti <sub>3</sub> O <sub>7</sub>	Structure of exfoliated/restacked Na(x)-[Ti <sub>3</sub> O <sub>7</sub> ] compositions	<sup>1</sup> H (Hahn-echo) and <sup>23</sup> Na (single-pulse) MAS SS-NMR	700 MHz 55-60 kHz	<sup>1</sup> H: 11.3 and 13.1 ppm (H <sub>2</sub> Ti <sub>3</sub> O <sub>7</sub> ) <sup>23</sup> Na: -10 and + 3 ppm (Na1 and Na2 sites in Na(x)-[Ti <sub>3</sub> O <sub>7</sub> ])	[73]



**Fig. 8.** Composition analysis of SEI. (a) (i)  $^{23}\text{Na}$  and (ii)  $^{11}\text{B}$  1D SS-NMR spectra of the SEI in the NaDFOB-based symmetric cells, (iii)  $^{23}\text{Na}$  and (iv)  $^{11}\text{B}$  2D 3QMAS NMR spectra of the NaDFOB-derived SEI. Reproduced with permission from [82]. (b) (i)  $^{23}\text{Na}$  and (ii)  $^{11}\text{B}$  SS-NMR spectra of SEI species harvested from the Na metal surface after the 15th, 50th, 100th, and 200th cycles. Reproduced with permission from [83]. (c) Single-pulse  $^{23}\text{Na}$  NMR and  $^1\text{H}\rightarrow^{23}\text{Na}$  CPMAS NMR spectra of SEI species harvested from Cu foil after 50 cycles, and the reference spectra of NaF and NaH. Reproduced with permission from [65]. (d) Ex-situ  $^{23}\text{Na}$  MAS NMR spectra of electrodes at different sodiation states in ILs. Reproduced with permission from [85].



**Fig. 9.** Characterization of electrolytes and ILs. (a) Diffusion coefficients ( $D$ ) of  $^1\text{H}$  and  $^{19}\text{F}$  with different NaFSI concentrations in [HMG][FSI] measured by PFG NMR as a function of temperature. Reproduced with permission from [87]. (b)  $^{23}\text{Na}$  NMR spectra vs. temperature (25 °C, 30 °C, 35 °C, 40 °C, 50 °C, and 60 °C) for the (i) line broadening (Full Width at Half Maximum, FWHM) and (ii) chemical shift. Reproduced with permission from [88].

In summary, SS-NMR can effectively characterize the amorphous anode materials and possible amorphous intermediate products during the cycling process. It also provides richer characterization information for speculating and in-depth understanding of the electrode sodiation mechanism. Moreover, in-situ/operando SS-NMR and MRI can quantitatively and non-invasively visualize the growth of SMSs on the electrode surface, which is a great tool for the design and modification of the anode materials (Table 2).

### 3. Solid electrolyte interfaces and electrolytes

In SIBs, complex contacts and reactions in different materials form various electrode–electrolyte interfaces (EEI), including liquid–solid and solid–solid interfaces. At the surface of reducing

(negative) and oxidizing (positive) electrodes, the solvent and sodium salt in the electrolyte inevitably decomposes to form an interfacial layer with complex composition, namely solid electrolyte interfaces (SEI) and cathode electrolyte interfaces (CEI). Several components can effectively promote the transport of  $\text{Na}^+$  and prevent the electron transport, which can inhibit the uncontrolled decomposition of the electrolytes. The chemical and physical properties of SEI greatly affect the cycling performance and lifetime of SIBs. Therefore, a comprehensive understanding of the composition, structure, and chemical properties of SEI and electrolytes will be of great significance for the development of improved electrochemical cycling performance SIBs.

However, SEI mostly has the following properties: i) complex polyphaser, ii) microscale, iii) amorphous, iv) sensitive to water and air. Plus,  $\text{Na}^+$  diffusion in the electrolyte and EEI is also com-

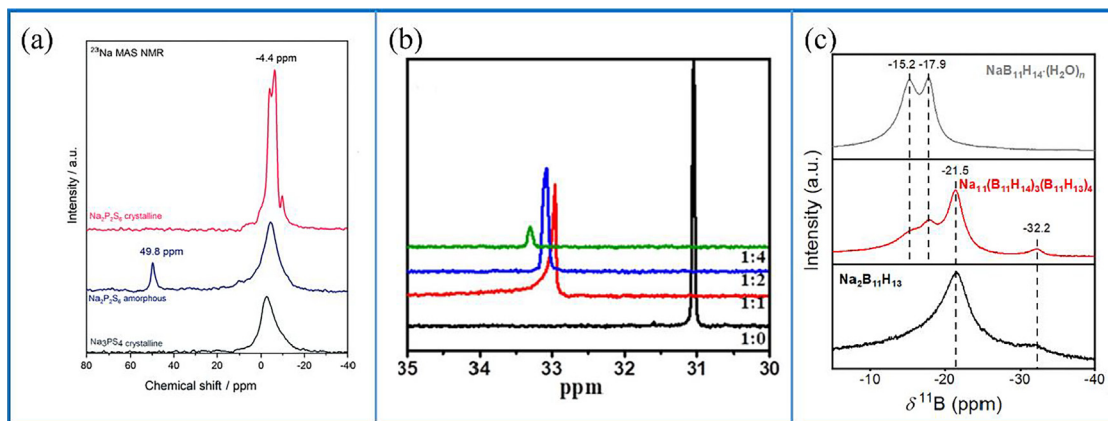


**Fig. 10.** Phase and chemical environment characterization of SSEs. (a)  $^{23}\text{Na}$  MAS NMR spectra of amorphous and crystalline  $\text{Na}_2\text{P}_2\text{S}_6$  and  $\text{Na}_3\text{PS}_4$ . Reproduced with permission from [89]. (b)  $^{31}\text{P}$  NMR spectra of MADEMP in the mixture solution of monomers and the LE with GPE1 system. Reproduced with permission from [90]. (c)  $^{11}\text{B}$  SS-NMR spectra of  $\text{NaB}_{11}\text{H}_{14}(\text{H}_2\text{O})_n$ ,  $\text{Na}_{11}(\text{B}_{11}\text{H}_{14})_3(\text{B}_{11}\text{H}_{13})_4$  and  $\text{Na}_2\text{B}_{11}\text{H}_{13}$  at room temperature. Reproduced with permission from [18].

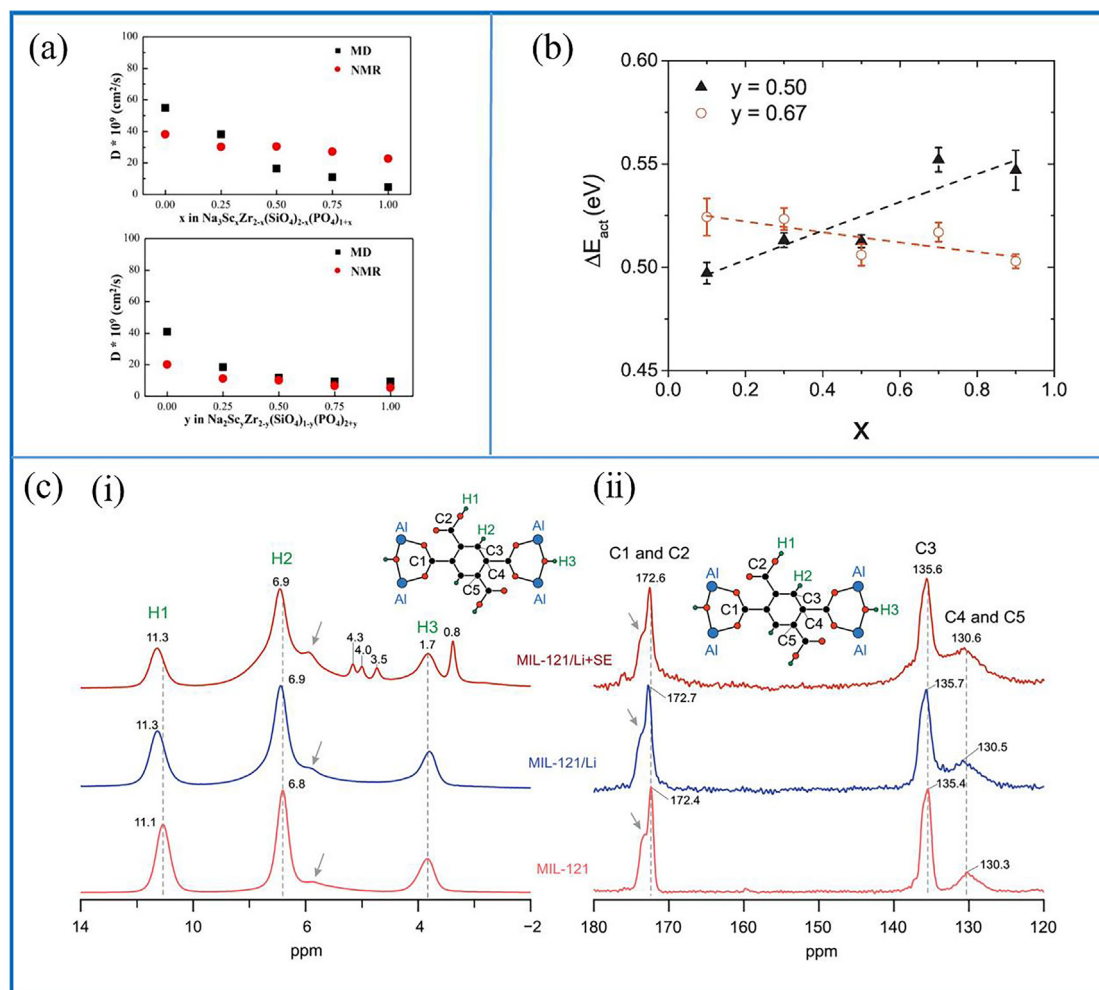


**Fig. 11.** Measurements of  $\text{Na}^+$  ion diffusion in different SSEs. (a) Diffusion coefficient  $D^T$  was obtained from NMR and the chemical diffusion coefficient  $D_c$  was calculated from MD simulations. Reproduced with permission from [96]. (b)  $^{23}\text{Na}$  average barrier energy  $\Delta E_{\text{act}}$  determined by NMR for  $y\text{Na}_2\text{S} + (1 - y)[x\text{SiS}_2 + (1 - x)\text{PS}_{2.5}]$  glasses for  $y = 0.50, 0.67$  and  $x = 0.1, 0.3, 0.5, 0.7,$  and  $0.9$ . Reproduced with permission from [97]. (c) (i)  $^1\text{H}$  MAS NMR spectra and (ii)  $^1\text{H}$ - $^{13}\text{C}$  CP MAS NMR spectra of MIL-121, MIL-121/Li, and MIL-121 + SE. Reproduced with permission from [99].

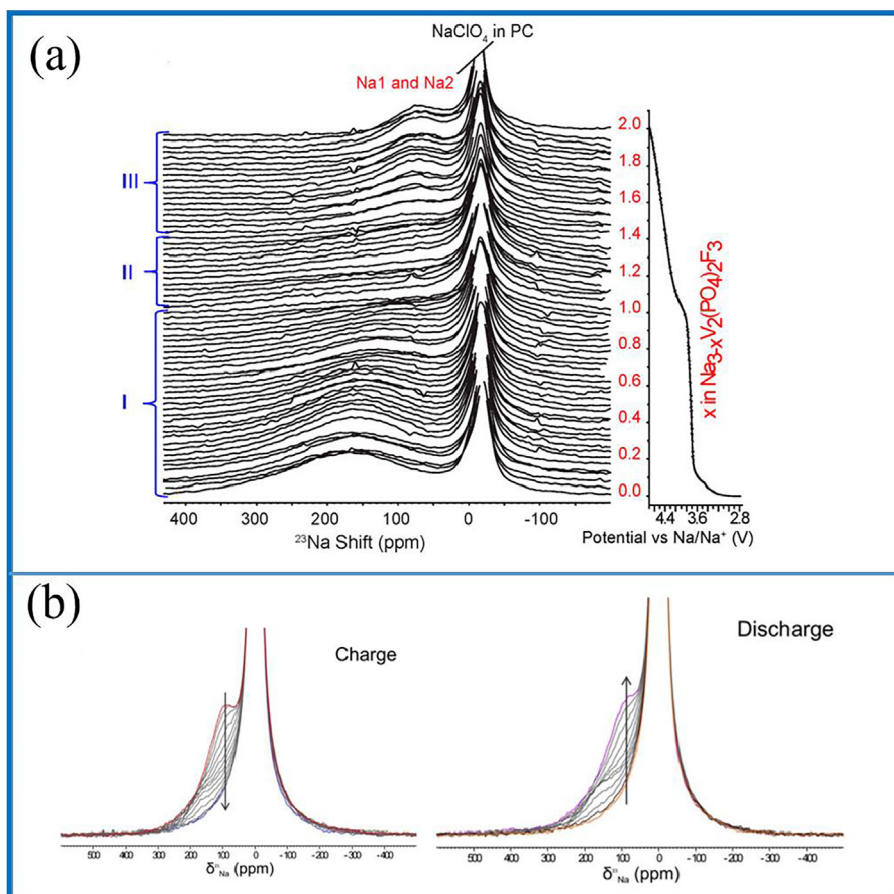


**Fig. 12.** In-situ NMR characterization in cathode materials. (a) In-situ  $^{23}\text{Na}$  NMR spectra ( $-150$  ppm to  $430$  ppm) obtained from a  $\text{Na}||\text{Na}_3\text{V}_2(\text{PO}_4)_2\text{F}_3$  bag-cell battery cycled at a current rate of  $C/100$  over the voltage window of  $2.5$  to  $4.5$  V. Reproduced with permission from [26]. (b) In-situ  $^{23}\text{Na}$  NMR spectra of  $\text{Na}||\text{NV}^{3.8}\text{POF}$  cell cycled at a current rate of  $0.05C$  during the first charge and discharge processes. Reproduced with permission from [43].

plex. In recent years,  $^{23}\text{Na}$  SS-NMR has become a powerful tool for analyzing the SEI compositions and ionic diffusion at the atomic level.

### 3.1. SEI composition characterization

SEI components mainly come from the decomposition of electrolytes, so their elemental composition is similar to that in the electrolyte solvents and sodium salts, i.e., containing Na, F, C, P, etc. Compared with XPS, SS-NMR can directly characterize the SEI components with different electrolytes and cycling processes.

Among the various anode materials, the SEI on the sodium metal anodes has been more deeply characterized. Gao et al. first discovered the excellent compatibility between the sodium-difluoro(oxalato)borate ( $\text{NaDFOB}$ )-based carbonate-ester electrolytes and sodium metal anodes.[82]  $^{23}\text{Na}$  and  $^{11}\text{B}$  3QMAS SS-NMR proposed the existence of  $\text{Na}_2\text{CO}_3$ ,  $\text{NaOH}$ ,  $\text{NaBF}_4$ , and  $\text{Na}_4\text{B}_2\text{O}_5$ , as well as the residual sodium salt  $\text{NaDFOB}$ .  $^{19}\text{F}$  SS-NMR found another important component,  $\text{NaF}$  in the SEI (Fig. 8a). Gao et al. further proved that the mechanism of SEI formation in  $\text{NaDFOB}$  and carbonate-ester solvents was different from that of the organic solvent decomposition of traditional electrolytes.  $^1\text{H}$ ,  $^{11}\text{B}$ , and  $^{19}\text{F}$  in-situ NMR results indicated that the SEI was completely decomposed by  $\text{NaDFOB}$  rather than organic solvents during the cycling process.  $^{23}\text{Na}$  and  $^{11}\text{B}$  3QMAS NMR further revealed the composition changes of  $\text{Na}_2\text{CO}_3$ ,  $\text{Na}_2\text{C}_2\text{O}_4$ ,  $\text{NaF}$ ,  $\text{NaOH}$ ,  $\text{NaBF}_4$ , and  $\text{Na}_4\text{B}_2\text{O}_5$  in the SEI (Fig. 8b).[83] In addition, Xiang et al. first reported the existence of  $\text{NaH}$  on the surface of sodium metal anodes by  $^{23}\text{Na}$  MAS SS-NMR and  $^1\text{H}$ - $^{23}\text{Na}$  CP MAS NMR (Fig. 8c).[65].

Apart from sodium metal anodes, Munoz-Marquez et al. first observed the unstable SEI formed in  $\text{Na}_2\text{Ti}_3\text{O}_7$  electrodes.  $^{19}\text{F}$  MAS SS-NMR proved that a part of  $\text{NaF}$  originated from the decomposition of the binder polyvinylidene difluoride (PVdF) at low voltage.[84] Also, Sun et al. investigated the excellent interfacial compatibility of ionic liquids (ILs) such as  $\text{NaFSI}/\text{N}$ -methyl- $\text{N}$ -propylpyrrolidinium bis(fluoromethane) sulfonamide ( $\text{C}_3\text{mpyrFSI}$ ) with carbon electrodes. The  $^{19}\text{F}$  and  $^{23}\text{Na}$  MAS NMR results suggested the formation of  $\text{NaF}$ -rich SEI (Fig. 8d).[85].

### 3.2. Electrolytes and ionic liquids

SS-NMR is rarely applied to the research of electrolyte composition, but in some specific systems, such as the  $\text{Na}^+$  diffusion in the ionic liquids, SS-NMR can get a wealth of information. Forsyth et al. analyzed the transport in the  $[x \text{ mol}\% \text{NaFSI}]-\text{C}_3\text{mpyrFSI}$  IL electrolytes via  $^{23}\text{Na}$  pulsed-field gradient (PFG)-NMR and proved the best cycling performance taking place in the  $x = 50$  electrolyte.[86] Biernacka et al. first found the higher diffusion coefficients of anion over cation in  $\text{NaFSI}$ -based Hexamethylguanidinium bis(fluorosulfonyl)imide ([HMG]FSI) IL electrolytes, which was different from the mixture of  $\text{LiTFSI}/\text{LiFSI}$  and [HMG]FSI. For the various ions, VT  $^{23}\text{Na}$ ,  $^1\text{H}$  ([HMG] $^+$ ),  $^{19}\text{F}$  (FSI $^-$ ) SS-NMR, and PFG-NMR results reaffirmed this conclusion (Fig. 9a).[87] Recently, Stigliano et al. distinguished the diffusion behavior of  $\text{Na}^+$  in two different chemical environments ( $\text{Na}$  (1)-mobile  $\text{Na}^+$  and  $\text{Na}$  (2)-involved in clusters or interacting networks) in  $\text{Pyr}_{13}\text{TFSI}-\text{NaFSI}$  via VT  $^{23}\text{Na}$  SS-NMR and  $^{23}\text{Na}$  PFG-NMR (Fig. 9b).[88].

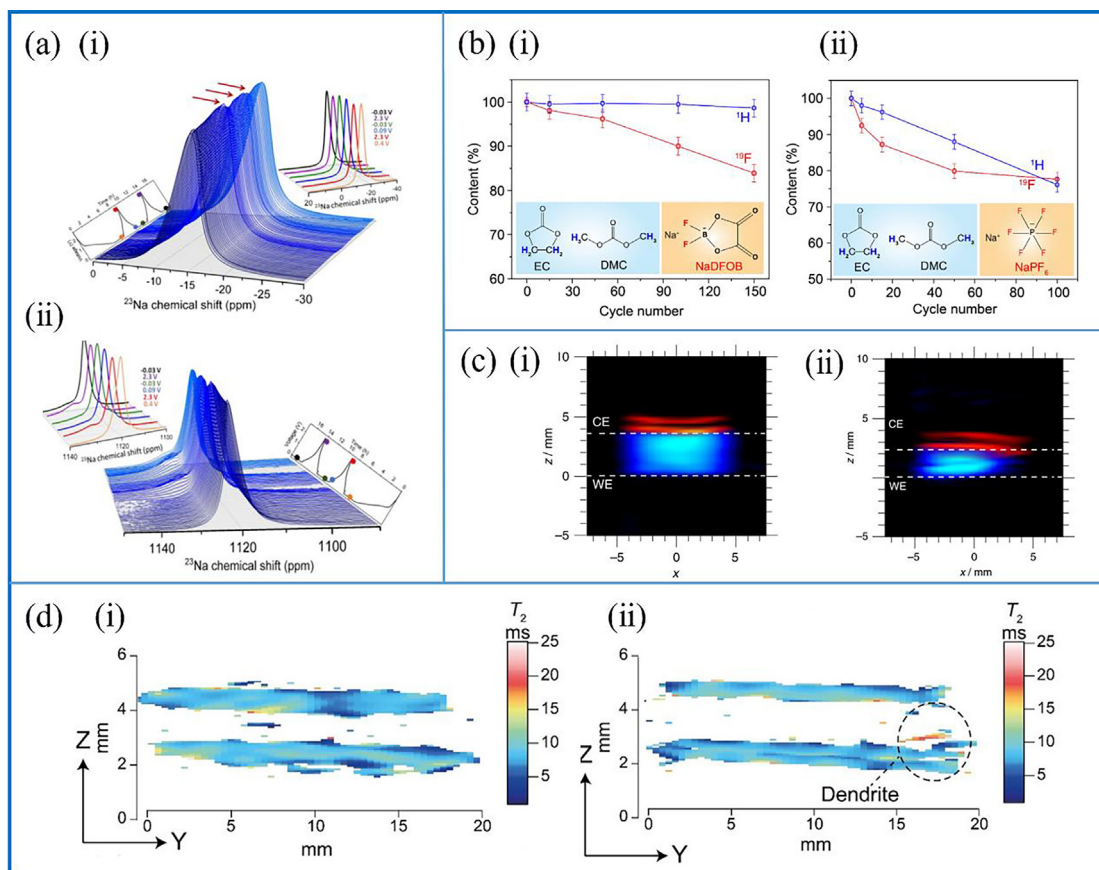


**Fig. 13.** Applications of in-situ NMR and MRI. (a) Enlarged 3D view of the  $^{23}\text{Na}$  in-situ NMR spectra of the (i) electrolyte region (0 to -30 ppm) and (ii) metal region (1150 to 1090 ppm) for the Na|NaPF<sub>6</sub>|SiCN cell. Reproduced with permission from [77]. (b) In-situ NMR measurements on a Na|Na cylindrical cell using (i) 1.0 M NaDFOB/EC:DMC and (ii) 1.0 NaPF<sub>6</sub>/EC:DMC electrolytes. Reproduced with permission from [83]. (c) 2D  $^{23}\text{Na}$  MRI of metallic (red) and dielectric (blue) sodium in the cell of (i) pristine sodium metal and (ii) after a single charge-discharge (30 mA g<sup>-1</sup>) cycle. Reproduced with permission from [104]. (d) The  $T_2$  weighted contrast maps of (i) the pristine symmetrical cell and (ii) the cell after short-circuits. Reproduced with permission from [105]. (For interpretation of the references to colour in this figure legend, the reader is referred to the web version of this article.)

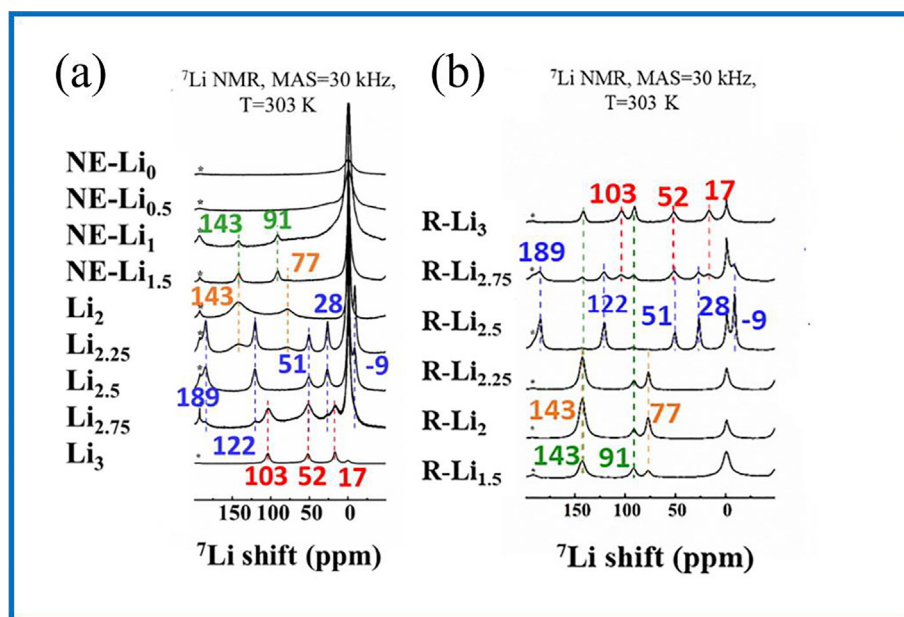


**Fig. 14.** Ex-situ  $^7\text{Li}$  MAS NMR spectra of  $\text{Li}_3\text{V}_2(\text{PO}_4)_3$  during (a) the first charge process within the electrochemical window of 3.0–4.8 V and (b) the first discharge process within the electrochemical window of 4.3–3.0 V. Reproduced and adapted with permission from [111].

**Table 3**  
NMR properties of  $^{23}\text{Na}$ ,  $^6\text{Li}$  and  $^7\text{Li}$ .

Nucleus	I	Natural abundance	NMR frequency at 9.4 T (MHz)	Relative receptivity	Quadrupole moment (mb)
$^6\text{Li}$	1	7.42%	58.89	$2.93 \times 10^{-2}$	-0.808
$^7\text{Li}$	3/2	92.5%	155.5	1.00	-40.1
$^{23}\text{Na}$	3/2	100%	105.9	0.341	104

### 3.3. Solid-state electrolytes (SSEs)

SSEs and all-solid-state sodium batteries can further improve the safety and energy density of SIBs. An in-depth understanding of the structure and  $\text{Na}^+$  transport mechanism of SSEs is the basis for the development of SSEs with good electrochemical cycling performance. In this section, we will summarize the SS-NMR applications in the study of phase characterization, chemical environment, and the ion transport mechanism.

#### 3.3.1. Phase and chemical environment

As for the most basic application of SS-NMR, phase characterization provides the information on composition, purity, and structure of SSEs. Some SSEs are sensitive to air and water, such as sulfide SSEs and polymer SSEs. Compared with ordinary XRD, SS-NMR allows the SSE samples to be effectively isolated from air during the characterization. In recent years, Fritsch et al. discerned the changes in the Na and P atom local environment of  $\text{Na}_2\text{S}_2\text{P}_6$  via  $^{23}\text{Na}$  and  $^{31}\text{P}$  MAS SS-NMR to differentiate various P-S tetrahedrals (Fig. 10a).[89] Zheng et al. investigated the interaction between gel polymer electrolytes and sodium ions in the different molar ratios of di(2-methylacryloyldioxyethyl)methyl phosphonate (MADEMP) in MADEMP-(acryloyloxyethyl) diethyl phosphates (AEDEP)-ethyl acrylate (EA) (GPE1) to  $\text{Na}^+$  via  $^{31}\text{P}$  SS-NMR spectroscopy (Fig. 10b).[90] Santhoshkumar et al. analyzed the local structure of  $\text{SiO}_4$ ,  $\text{PO}_4$ , and different phases of composite samples (NASICON-type  $\text{Na}_3\text{Zr}_2\text{Si}_2\text{PO}_{12}/\text{Na}_2\text{Si}_2\text{O}_5$ ) via  $^{31}\text{P}$  and  $^{29}\text{Si}$  MAS SS-NMR.[91] Keshri et al. observed the  $\text{Ag}^+-\text{Na}^+$  ion exchange and structure of  $\text{Na}_3\text{Al}_{1.8}\text{Si}_{1.65}\text{P}_{1.8}\text{O}_{12}$  glass electrode via  $^{23}\text{Na}$ ,  $^{27}\text{Al}$ ,  $^{29}\text{Si}$ ,  $^{31}\text{P}$  MAS SS-NMR and  $^{23}\text{Na}$ ,  $^{27}\text{Al}$  MQ MAS SS-NMR.[92] SS-NMR has also been applied to the structural characterization of new solid electrolyte materials, such as  $\text{Na}_2\text{B}_{11}\text{H}_{13}$  and  $\text{Na}_{11}(\text{B}_{11}\text{H}_{14})_3(\text{B}_{11}\text{H}_{13})_4$  via  $^{11}\text{B}$  MAS NMR (Fig. 10c).[18].

#### 3.3.2. $\text{Na}^+$ ion diffusion processes

SS-NMR can uniquely characterize the kinetic processes of  $\text{Na}^+$  in SSEs, such as the ion diffusion mechanism. In particular, the ion diffusion coefficient can be directly determined by the VT and PFG SS-NMR.[93] SS-NMR has been widely used to study the ionic transport mechanism of  $\text{Li}^+$  in SSEs[94,95], but not in the sodium-based SSEs. In recent years, Deng et al. determined the  $^{23}\text{Na}$ - $T_1$  relaxation times of NASICON-type  $\text{Na}_3\text{Sc}_x\text{Zr}_{2-x}(\text{SiO}_4)_2-x(\text{PO}_4)_{1+x}$  ( $\text{N3}$ ,  $0 < x < 1$ ) and  $\text{Na}_2\text{Sc}_y\text{Zr}_{2-y}(\text{SiO}_4)_{1-y}(\text{PO}_4)_{2+y}$  ( $\text{N2}$ ,  $0 < y < 1$ ) at different temperatures and proposed the 3D diffusion pathway of  $\text{Na}^+$  in the NASICON-type materials (Fig. 11a).[96] Combined with the molecular dynamics (MD), bond valence, and maximum entropy methods,  $^{23}\text{Na}$  SS-NMR revealed the 3D diffusion pathway (consisted of several 2D local hops) with  $\text{Na}^+$  continuously exchanged between the Na (1) and Na (2) sites. Shastri et al. performed the Gaussian distribution of activation energies and mean barrier values in the  $y\text{Na}_2\text{S} + (1-y)[x\text{SiS}_2 + (1-x)\text{PS}_{2.5}]$  via the FWHM and  $T_1$  in VT  $^{23}\text{Na}$  SS-NMR spectra (Fig. 11b).[97]  $^{23}\text{Na}$  NMR second moment results suggested that the spatial arrangement of cations was uniformly distributed over most of the composition range in the  $y = 0.5$  and  $0.65$  samples. Simari et al. reported the Na-Nafion membrane (NNM) for the sodium metal aprotic batteries, indicating two distinct  $\text{Na}^+$  populations

from the  $^{23}\text{Na}$  MAS SS-NMR and  $^{23}\text{Na}$ - $T_1$  measurements, corresponding to the  $\text{Na}^+$  either combined with the anionic sulfonic groups or coordinated by the carbonate molecules. The  $\text{Na}^+$  diffusion coefficient in solid polymer electrolyte was firstly measured via PFG-NMR ( $5 \times 10^{-7}\text{mS cm}^{-2}$ ,  $30^\circ\text{C}$  to  $1 \times 10^{-6}\text{mS cm}^{-2}$ ,  $60^\circ\text{C}$ ). [98] In addition, Zettl et al. reported a metal-organic framework (MOF)-based MIL-121 SSEs with  $\text{Li}^+$  and  $\text{Na}^+$ . [99] They observed the crossover from the correlated to the uncorrelated motion at higher temperature by  $^7\text{Li}$  and  $^{23}\text{Na}$  NMR spin-lattice relaxation, and the significantly lower activation energy for  $\text{Li}^+$  hopping upon adding soaking electrolytes.  $^1\text{H}$  MAS SS-NMR and  $^1\text{H}$ - $^{13}\text{C}$  CP MAS NMR results showed that the main charge carrier was  $\text{Li}^+$  in Li-bearing MOF (Fig. 11c). In addition,  $^{23}\text{Na}$ - $T_1$  relaxation times for Sc-doped NASICON-type  $\text{Na}_3\text{Zr}_2\text{Si}_2\text{PO}_{12}$  proposed the effect of  $\text{Sc}^{3+}$  on the local structure (Na (1), Na (2) and, Na (3)).[100].

## 4. In-situ NMR and MRI characterization

Cells, considered as a black-box, have abundant non-disclosed electrochemical or chemical reactions and intermediate phases during operations. Ex-situ SS-NMR characterization requires pausing the electrochemical cycling and dismantling of the cells, which leads to the rapid reaction or self-relaxation of intermediate phases and loss of electrochemical information. In-situ SS-NMR and MRI techniques can make up for obtaining more real-time and dynamic information inside the cells, such as unstable chemical species, amorphous materials, ionic diffusion, and so on. In addition, in-situ MRI, with the magnetic field gradients, provides higher spatial resolution, concrete and intuitive information in real-time. Therefore, these characterization techniques are powerful for deep understanding of the electrochemical reaction mechanism, revealing the failure of SIBs thus leading to improve their cycling performance. At present, in-situ SS-NMR and MRI have been widely applied in LIBs[101–103], but far fewer studies focus on the SIBs. In this section, we will summarize the applications of in-situ NMR and MRI in SIBs.

Due to the limited resolution under static conditions, in-situ SS-NMR and MRI techniques are rarely applied to the characterization of cathode materials. Liu et al. investigated the structural and dynamical changes of  $\text{Na}_3\text{V}_2(\text{PO}_4)_2\text{F}_3$  during the charging process via in-situ  $^{23}\text{Na}$  SS-NMR and proved the three different stages of charging with different  $\text{Na}^+$  electronic mobility and vanadium electronic configurations (Fig. 12a).[26] Li et al. probed the structural evolution of  $\text{Na}_3\text{V}_2(\text{PO}_4)_2\text{O}_{1.6}\text{F}_{1.4}$  ( $\text{NV}^{+3.8}\text{POF}$ ) during the cycling process via operando  $^{23}\text{Na}$  SS-NMR. The reduction (charging process) and recovery (discharging process) of the broad signal peak at 90 ppm showed the reversibility of the electrochemical cycling process (Fig. 12b).[43].

More research focus on the anode materials, especially sodium metal anodes, hard carbon, and Si-based anodes. The applications in sodium metal anodes and SEI characterization have been comprehensively summarized in Sections 2.2.3 and 3.1. Šić et al. proved the reversible structural evolution of SiCN anodes during the cycling processes and the formation of the sodium dendrite growth when the voltage was increased to 2.5 V.[77]  $^{23}\text{Na}$  in-situ SS-NMR results showed the consecutive and reversible intensity fluctuations of the signals at -13 ppm (electrolyte) and 1120 ppm

(sodium metal). It was conducive to understanding the structural evolution and the formation of SEI, sodium metal, and sodium dendrites with the  $\text{Na}^+$  diffusion in these materials (Fig. 13a). Gao et al. first demonstrated the decomposition of NaDFOB, instead of electrolyte solvent, to form a stable SEI via in-situ SS-NMR (Fig. 13b). [83] Bray et al. first developed the visible electrochemical analytical methods of the electrodes and electrolytes in hard carbon via operando  $^{23}\text{Na}$  SS-NMR and  $^{23}\text{Na}/^1\text{H}$  MRI (Fig. 13c). [104] They proved the formation of sodium metal during the first cycle and electrochemical changes of sodium species in the cells and laid the foundation for further understanding the electrochemical reaction mechanism of other materials. As for the solid-state electrolytes, Rees et al. reported the applications of  $T_2$ -weighted MRI to characterize the growth of sodium microstructures in the all-solid-state batteries (Fig. 13d). [105] The  $T_2$  of sodium dendrites was significantly longer than the bulk sodium metal, due to the higher mobility of dendrites. Combined with the X-ray and microscope-based characterization, the  $^{23}\text{Na}$   $T_2$ -weighted MRI obtained an extra method of characterizing the microstructure growths, dendritic, and crack formations. In the future, in-situ NMR and MRI techniques will be attractive and suitable for other electrodes and electrolytes.

### 5. Comparison of $^{23}\text{Na}$ and $^6\text{Li}$ NMR/MRI techniques in batteries

As far as we know, with the effect of the quadrupole interaction,  $^{23}\text{Na}$  SS-NMR spectra show broader signals as compared to  $^6\text{Li}/^7\text{Li}$  NMR which makes the  $^{23}\text{Na}$  NMR spectra more complex. [106,107] Although  $^{23}\text{Na}$  has near 100% natural abundance, its sensitivity is still lower than  $^7\text{Li}$  due to their difference in receptivity. Table 3 lists the NMR properties of  $^{23}\text{Na}$ ,  $^6\text{Li}$ , and  $^7\text{Li}$ . Some papers have considered the differences in the electrodes and interfaces between SIBs and LIBs, such as the difference in crystal structure [5], metal anode [108], and SEI [109], etc. However, few researchers have focused on the SS-NMR spectrum differences of lithium/sodium in similar material systems in SIBs or LIBs. A better understanding of the differences in SS-NMR spectra between similar materials of SIBs and LIBs may contribute to the further development and optimization of novel materials. In this section, with a comparison of the SS-NMR spectra and methods of Na and Li in similar materials, we hope to stimulate some new ideas for subsequent research.

**Material characterizations.** Due to the different crystal structures of various Na/Li-based materials, the ionic migration in the materials experiences distinctly different processes. SS-NMR can effectively capture information of local structure evolution in similar types of cathode materials in SIBs and LIBs. The chemical shifts of cathode materials are mainly affected by the hyperfine interactions of TM ions. Taking the monoclinic  $\text{Na}_3\text{V}_2(\text{PO}_4)_3$  and rhombohedral  $\text{Li}_3\text{V}_2(\text{PO}_4)_3$  as examples, as mentioned in Section 2.2,  $^{23}\text{Na}$  SS-NMR confirmed the reversible cycling performance of  $\text{Na}_3\text{V}_2(\text{PO}_4)_3$ , and the signals at  $\sim 223$  ppm and  $-137$  ppm in the charging process respectively corresponded to the hyperfine interaction of  $\text{V}^{4+}$  and  $\text{V}^{2+}$ . [27] However, in the previous work, the surface of pristine  $\text{Li}_3\text{V}_2(\text{PO}_4)_3$  was composed of  $\text{V}^{5+}$ ,  $\text{V}^{4+}$ , and  $\text{V}^{3+}$ , but  $\text{V}^{5+}$  was not found on the surface of pristine  $\text{Na}_3\text{V}_2(\text{PO}_4)_3$  by XPS, which indicated the different distribution of  $\text{M}^+$  and crystal structures in  $\text{M}_3\text{V}_2(\text{PO}_4)_3$  ( $\text{M} = \text{Li}^+$  or  $\text{Na}^+$ ). [110]  $^7\text{Li}$  MAS SS-NMR showed the three chemical shifts at 103, 52, and 17 ppm in  $\text{Li}_3\text{V}_2(\text{PO}_4)_3$ . Unlike  $\text{Na}_3\text{V}_2(\text{PO}_4)_3$ ,  $\text{Li}_3\text{V}_2(\text{PO}_4)_3$  showed a complex electrochemical mechanism of structure evolution, especially in the kinetically difficult process between  $\text{Li}_2\text{V}_2(\text{PO}_4)_3$  and  $\text{V}_2(\text{PO}_4)_3$ . The signals at 143 and 91 ppm corresponded to the distorted structures of Li sites in  $\text{Li}_2\text{V}_2(\text{PO}_4)_3$ , which exhibited irreversible structural deformation

**Table 4**  
NMR methods and corresponding applications in sodium batteries.

NMR techniques	Applications	Representative Examples	Ref.
Magic-angle spinning, <b>MAS</b>	Narrow line-width of signal for high-resolution spectra.	A usual experimental condition applied in almost all components.	[44]
Cross-polarization, <b>CP</b>	Increase the sensitivity of low-abundance nuclei	Interfaces: soft carbon.	[79]
Projection of magic-angle turning phased-adjusted sideband separation, <b>pmjMATPASS</b>	Sperate the overlapping main peaks and sidebands to identify the main resonances.	Paramagnetic cathodes	[16]
Pulsed-field gradient, <b>PFG</b>	Collect self-diffusion coefficients to obtain kinetic information about ions diffusion, and applied to MRI.	Solid state electrolyte (SSE): [HMG]FSI	[87]
Two-dimensional exchange spectroscopy, <b>2D-EXSY</b>	Provide quantitative data about ion transport processes.	Cathode: $\text{Na}_2\text{FePO}_4\text{F}$	[42]
Dynamic Nuclear Polarization, <b>DNP</b>	Increase the sensitivity of NMR signals.	Anodes and Interfaces (expect)	[121]
<b>In-situ NMR</b>	Capture metastable structures and collect real-time information.	Cathode: $\text{Na}_3\text{V}_2(\text{PO}_4)_2\text{F}_3$ Anode: Sodium metal Electrolyte: NaDFOB	[26,64,83]
Magnetic Resonance Imaging, <b>MRI</b>	Visualize the spatial distribution of signals.	Anodes: sodium metal, hard carbon.	[65,104]
Variable temperature, <b>VT</b>	Acquire information such as ionic mobility to evaluate ion dynamics.	Anode: Sb. SSE: $\text{NaZr}_2(\text{PO}_4)_3$	[66,122]
Rotational-echo double-resonance, <b>REDOR</b>	Determine the internuclear distances.	Cathode: S-NMO	[17]

during the cycling processes (Fig. 14). [111] The differences of  $^{23}\text{Na}/^7\text{Li}$  SS-NMR spectra represent the various kinetics electrochemical mechanisms, structural evolutions, and cycling reversibility of  $\text{Na}_3\text{V}_2(\text{PO}_4)_3$  and  $\text{Li}_3\text{V}_2(\text{PO}_4)_3$ . Therefore, comparing the SS-NMR spectra of similar species contributes to a deep understanding of Li-doped cathode materials and novel materials in SIBs.

**SS-NMR spectroscopy.** Rich experimental methods in SS-NMR provide effective information in SIBs. As for the sodium metal anodes, the chemical shifts of anode materials are mainly affected by the Knight shift, which come from the interaction of nuclear spins with electrons in the conductors or semiconductors. Especially in the metal anodes, the chemical shifts of sodium metal ( $\sim 1130$  ppm) and lithium metal ( $\sim 250$  ppm) are quite different, while the chemical shifts of their SEI are both close to 0 ppm. Such a large Knight shift of sodium metal requires a wide excitation bandwidth for SS-NMR to detect all sodium signals, which may pose extra difficulties to the in-situ NMR and MRI experiments. As for the solid-state electrolytes, unfortunately, because the  $^{23}\text{Na}$  is the sole stable isotope, the experiments like  $^6\text{Li}/^7\text{Li}$  tracer-exchange [112] are out of question for SIBs. In addition, short  $T_1$  and  $T_2$  of  $^{23}\text{Na}$  result in the poor signal to noise ratio in PFG-NMR experiments and thus it becomes hard to accurately determine the  $\text{Na}^+$  diffusion coefficient in sodium solid-state

electrolytes.[113] Nowadays, the SS-NMR techniques in LIBs have been developed rapidly, and great progress has been made in the research of the morphology, surface composition, and  $\text{Li}^+$  diffusion mechanism of lithium metal anodes, such as the dissolution of lithium metal via  $^7\text{Li}$  in-situ SS-NMR.[114] In the future, by adapting the SS-NMR experimental methods and pulse sequences developed in LIBs[10],  $^{23}\text{Na}$  SS-NMR could provide more effective information for the electrode materials in SIBs.

## 6. What can we learn from SS-NMR in SIBs?

As a non-destructive and quantitative spectroscopic characterization method, SS-NMR has been widely applied to characterize various solid materials, including organic, inorganic, amorphous, and crystalline materials. The anisotropic interactions in solid materials provide rich chemical and local structural information. However, the complex low-resolution SS-NMR spectra make it difficult to interpret the structural information in different systems. For example, the hyperfine interaction between the 3d/4d unpaired electrons of the TM and the Na nuclei in paramagnetic materials leads to broad peaks and dramatically complicates the obtained  $^{23}\text{Na}$  SS-NMR spectrum, but it contains some information of spatial location and orientation of TM ions in the lattice structure.

In recent years, several articles have focused on the basic principles and experimental methods of SS-NMR, the advantages, and features of ex-situ/in-situ SS-NMR experiments[107], and the applications of SS-NMR in functional nanomaterials[115], LIBs[10], SIBs[11], and electrode–electrolyte interface[116]. Most of these articles and monographs have already detailed the main interactions in SS-NMR (such as chemical shielding, dipolar-dipole interactions, quadrupole interactions, etc.) [9]. In this section, we aim to discuss the experimental conditions and methods of SS-NMR in sodium-ion battery research and provide several selection bases for SS-NMR experiments in different materials and structures.

### 6.1. Overview of SS-NMR techniques in SIBs

**Magic-Angle Spinning (MAS).** As one of the most popular SS-NMR techniques, the working principle of MAS ( $\theta = 54.7^\circ$ , between the magnetic and rotation axis) has been extensively discussed. [107] High-resolution SS-NMR experiments generally require to use MAS. In practice, MAS often fails to completely remove anisotropy when the spinning is not fast enough, leading to a series of spin sidebands spaced at the rotational speed. Thus, paramagnetic materials in SIBs are mainly characterized at high speeds (Table 1). In addition, it is worth noting that eddy currents from high-speed rotation can significantly affect the chemical shift of those samples with high electronic conductivity (such as carbon-based materials).

**Relaxation Times  $T_1/T_2$ .** After disturbed by the applied RF, a nuclear spin deviate from its equilibrium state. The recovery from the non-equilibrium back to equilibrium state is governed by the relaxation processes. Among them, the spin–lattice relaxation time,  $T_1$ , corresponds to the process of energy transfer between the spin system and its surrounding medium. While the spin–spin relaxation time,  $T_2$  represents the internal energy transfer within the spin system. Measuring  $T_1$  and  $T_2$ , allows us to obtain various information such as ion-transfer kinetics, material structure, interface species composition, and so on. For example, when the  $^{23}\text{Na}$  ions in different chemical environments have different mobilities, they preserve their own relaxation behaviors. By measuring  $T_1$  of individual  $^{23}\text{Na}$  ion, we are able to characterize the local structure and ionic motion in solid-state electrolytes [117] and ionic liquids [88].

**Cross polarization (CP)** CP is the method of transferring the polarization of the high-abundance nucleus (such as  $^1\text{H}$ ,  $^{19}\text{F}$ ) to the low-abundance nucleus (such as  $^{13}\text{C}$ ,  $^{15}\text{N}$ ) primarily mediated by the dipole interactions between the two nuclei, thereby enhancing the signal of the low-abundance nucleus and significantly reducing the spectral acquisition time. Combined with MAS, the CP-MAS technique is a powerful tool for the determination of the charge–discharge mechanisms of the organic anode materials and quantitative analysis of nuclei in specific chemical environments in SIBs. In the future, the CP-MAS technique is expected to be used for the analysis of SEI composition and structure of SIBs.

**Two-dimensional exchange spectroscopy (2D-EXSY).** 2D-EXSY is the NMR scheme that has a mixing period sandwiched by two different time-domains (i.e.,  $t_1$  and  $t_2$  domains). The chemical shifts evolve in the two time-domains separately. However, when there exists a relatively slow chemical exchange between the ions with different chemical shifts, their signal intensities start to mutual exchange during the mixing period, resulting in cross peaks in the 2D spectrum. This is a powerful technique allowing to identify those ions that have different chemical environments but experience slow chemical exchange between them and to measure their exchange rate constants, if needed, by varying the mixing period. We can thus obtain the dynamic information of solid materials in SIBs from 2D-EXSY spectra, such as the ion migration mechanism and transport path.

**Pulsed-field gradient (PFG).** Different from conventional SS-NMR experiments conducted under a constant magnetic field, pulsed-field gradient enables further analysis of the spatial distribution of the nuclei of the target atom. In addition, combined with the VT and relaxation time measurement, the PFG technique can effectively determine kinetic information, such as ion mobility and ion migration path in solid electrolytes.

**Dynamic nuclear polarization (DNP).** The DNP technique is to polarize the spin energy level of the relevant nucleus through the interaction with electrons by irradiating the electrons. Thus, those SS-NMR signals from low-content components can be greatly enhanced. DNP has shown great advantages in the characterization of electrode–electrolyte interface components and structures of LIBs[118–120], and we look forward to the further applications of DNP in SIBs.

**In-situ NMR/MRI.** The advantages and application of in-situ NMR/MRI have been introduced in Section 4. In fact, by avoiding the exposure of air and the destruction of batteries, in-situ NMR/MRI can determine the metastable species and distribution of SIBs during cycling.

In addition to these techniques, several pulse sequences have been used to characterize various materials and structures in SIBs. For example, the projection of magic-angle turning phased-adjusted sideband separation (pj-MATPASS) is widely applied to separate the main peak and the sideband of paramagnetic materials in SIBs, while REDOR is used to determine the interactions and distance between specified nuclei. The methods and corresponding applications of SS-NMR in SIBs are summarized in Table 4.

### 6.2. Limitations of the SS-NMR techniques

Although the SS-NMR technique has become one of the most important characterization methods in SIBs, it is necessary to recognize several limits of SS-NMR in SIBs and move forward with future research on these limits.

**Pulse sequences for paramagnetic materials.** The short  $T_1/T_2$  and spectral complexities of some paramagnetic materials make it difficult to obtain well-defined local structure and dynamic information. Choosing the appropriate sequences to simplify the spectra, such as suppressing spinning sidebands in paramagnetic materials and similar chemical shifts of complex compositions in

SEI, can effectively enhance the resolution of SS-NMR characterization of paramagnetic materials. Therefore, the development of pulse sequences and simulations and calculations of SS-NMR for paramagnetic materials will be an important opportunity.

**Higher resolution/sensitivity.** To achieve higher resolution and sensitivity, the characterization of the SS-NMR technique requires more powder samples and longer experimental times (especially in the characterization of low abundance nuclei), which in turn limits the rotation speed and makes spectral analysis difficult. However, the high cost of the DNP technique or ultrahigh magnetic field makes it difficult to scale. It is worth thinking about how to further improve the resolution of SS-NMR techniques with economy methods.

**Quantitative analysis.** Quantitative analysis with NMR has been widely applied in liquid samples. However, limited by the broad peaks and identification difficulties, the advantages of SS-NMR in the quantitative analysis of SIBs have not been fully developed. In recent years, more and more articles have focused on the quantitative analysis of SEI[123], dead Li[114 124], and the failure mechanism[125] of lithium metal anodes via in-situ/ex-situ SS-NMR. Quantitative analysis of the evolution process of electrolytes in sodium metal anodes has also been reported [82,83]. Combined with other characterization techniques, such as ex-situ titration gas chromatography (TGC) and mass spectrometry titration (MST) techniques[125], quantitative analysis with SS-NMR can further study the evolution and failure mechanism of SIBs in the future. We believe the development of quantitative analysis methods for SS-NMR will be very useful.

## 7. Summary and perspective

Over the past decade, SIBs have made remarkable progress due to the cost advantage. SS-NMR techniques have greatly promoted the understanding of the material structure and ionic diffusion in SIBs, especially in amorphous materials. In this article, the advanced characterizations of SS-NMR in SIBs of cathode materials, anode materials, SEI, and solid-state electrolytes are systematically discussed with special attention to the application of in-situ NMR/MRI techniques. Nowadays, SS-NMR techniques have shown unique advantages in the study of local structure evolution[16], material phase change[26], Na-ion transport mechanisms[96], and surface component analysis[65]. To obtain non-destructive and real-time information, in-situ NMR/MRI techniques have also been applied in the formation of inactive sodium[65] and electrolytes[83], which have high chemical reactivity. The current research progress exhibits that the SS-NMR techniques have gradually become an indispensable tool in the characterization of SIBs. Furthermore, we summarized and analyzed the differences in spectra and methods between  $^{23}\text{Na}$  SS-NMR with  $^7\text{Li}/^6\text{Li}$  SS-NMR, which is helpful to deepen the understanding of the material structure and experimental methods in SS-NMR. However, the SS-NMR techniques of SIBs still encounter several difficulties such as in the spectral elucidation, accurate quantitative analysis of electrode interfacial components, high-resolution of in-situ NMR/MRI, etc. In addition, the combination of SS-NMR with other techniques (XRD, XPS, XAS, PDF, etc.) is an important means to comprehensively understand the key issues of SIBs.

For paramagnetic materials, paramagnetic ions and complex interactions complicate the SS-NMR spectroscopy. In sodium layered oxides, the structure and reaction of  $\text{O}^{2-}$  significantly affect the cycling stability of high voltage cathode materials. Unfortunately, due to the low natural abundance of  $^{17}\text{O}$  (0.04%, with low NMR sensitivity) and the complex interaction between the  $\text{O}^{2-}$  and paramagnetic TM ions,  $^{17}\text{O}$  SS-NMR and paramagnetic TM SS-NMR (such as  $^{55}\text{Mn}$ ) cannot be directly applied to the character-

ization of cathode materials. But based on the high magnetic fields SS-NMR[126], high speed MAS and  $^{17}\text{O}$  isotope labeling materials, the application of  $^{17}\text{O}$  SS-NMR in SIBs will be feasible in the future. [127] Furthermore, it is also important to quantitatively analyze the relationship between ion diffusion, structural or phase transition, and cycling stability of electrode materials with VT and PFG SS-NMR experiments. In addition, the combination of SS-NMR techniques with efficient theoretical calculations and simulations is conducive to achieving reliable peak identification and prediction of NMR spectra.[128,129] Lin et al. first calculated the chemical shifts and  $\text{Na}^+$  distribution of the various sites in the  $\text{P2-Na}_{2/3}(\text{Mg}_{1/3}\text{Mn}_{2/3})\text{O}_2$  via density functional theory (DFT) and deep potential molecular dynamics (DPMD)[130]. They then presented a machine learning (ML) model, based on the local structure descriptors and a Neural Network (NN) to predict the NMR chemical shift of paramagnetic materials  $\text{Na}_{2/3}(\text{Mg}_{1/3}\text{Mn}_{2/3})\text{O}_2$ . [131] Compared with other cathode materials, it is worth mentioning that there is still limited SS-NMR work on Prussian blue materials and their analogs in the literature. All in all, SS-NMR studies for new positive poles are still challenging.

Electrode-electrolyte interface is one of the key issues in the development of SIBs in the future. Due to the high reactivity of anode materials during the sodiation process, some dynamic information may be lost in the sample cleaning and loading which are required for the ex-situ SS-NMR experiments. For the research on SEI, due to the complex and trace composition, SS-NMR cannot distinguish them quickly and accurately. MQ MAS experiments (in weaker hyperfine interaction systems), pj-MATPASS (in stronger hyperfine interaction systems) and DNP technique (especially in low abundance nuclei, surfaces and interfaces of electrodes) can respectively improve the sensitivity and resolution of SS-NMR in different application orientations. In addition,  $^{23}\text{Na}$  PFG-NMR experiments have a poor signal-to-noise ratio, which is not conducive to an in-depth understanding of  $\text{Na}^+$  diffusion. Recently, first-principles phonon calculations were applied in the prediction of  $^{23}\text{Na}$  NMR chemical shift and  $\text{Na}^+$  diffusion mechanism in the solid-state electrolyte NASICON  $\text{NaZr}_2(\text{PO}_4)_3$  which exhibited the importance of combining NMR with theoretical calculations/simulations. In addition, research on electrolyte additives is gradually increasing. The characterization of special components in electrolytes, such as  $\text{SnCl}_2$ [132] and KTFSI[133], via  $^{119}\text{Sn}/^{39}\text{K}$  SS-NMR technique may be beneficial to understanding the formation and composition of SEI and CEI.

In-situ NMR and MRI exhibit great advantages and potential in non-destructive and quantitative analysis of the complex electrochemical mechanism in SIBs. However, in practical application, these technologies still need to overcome several challenges. Firstly, in general, the sample cannot be rotated, so that the nuclear interactions cannot be eliminated, thus broadening signals and lowering spectral resolution as compared to the ex-situ MAS SS-NMR, especially in the paramagnetic cathode materials. Freytag et al. demonstrated a new in situ MAS  $^7\text{Li}$  NMR strategy through a novel jelly roll cell design, which acquired adequate resolution to monitor the full lithium inventory during cycling.[134] However, only the 1/100C cycling rate of  $\text{LiCoO}_2/\text{graphite}$  cell has been achieved, and its electrochemical performance, cell structure (non-metallic current collectors), and spinning speed need to be further optimized. Secondly, various components correspond to the different chemical shifts, such as the sodium metal ( $\sim 1130$  ppm), sodium salt ( $\sim 0$  ppm), and cathode materials (broad signal peak). But the applied RF cannot effectively/uniformly excite the entire range[107], which leads to information loss and difficulty distinguishing the components which correspond to the similar chemical shifts. In addition, the metal shell in the common coin cells will prevent the RF from exciting the electrode materials and the NMR signal acquisition (called the "skin effect") [102]. The size of

common coin cells is also not suitable for in-situ SS-NMR and MRI coils. Nowadays, a mass of work focuses on the new types of in-situ cells, such as cylindrical cells and pouch cells, which require high tightness and ample electrical contact with electrode materials. Plus, it is also important to design the appropriate pulse sequence according to the cell structure to improve the resolution of In-situ NMR and MRI. The development of in-situ MAS NMR devices [134], high gradient magnetic field, and advanced pulse trains will possibly achieve high-resolution NMR signal acquisition in the in-situ NMR and MRI experiments.

In conclusion, SS-NMR has become an important technique in the characterization of SIBs, but it is yet to be a 'perfect' characterization technique. However, the rapid development of SIBs cannot be separated from the characterization support of SS-NMR techniques. We expect that the richer SS-NMR techniques will play a greater role in exploring complex electrochemical processes in SIBs at a different time/spatial scale.

### Data availability

No data was used for the research described in the article.

### Declaration of Competing Interest

The authors declare that they have no known competing financial interests or personal relationships that could have appeared to influence the work reported in this paper.

### Acknowledgements

This work is financially supported by National Natural Science Foundation of China (Grant No. 21935009) and the National Key R&D Program of China (Grant No. 2021YFB2401800). R.F. acknowledges the support from the National High Magnetic Field Lab supported by NSF Cooperative Agreement DMR-2128556 and the State of Florida. We would also like to thank Ms. Isabel Ruby for English polishing.

### References

- [1] M.D. Slater, D. Kim, E. Lee, C.S. Johnson, Sodium-ion batteries, *Adv. Funct. Mater.* 23 (2013) 947–958, <https://doi.org/10.1002/adfm.201200691>.
- [2] N. Yabuuchi, K. Kubota, M. Dahbi, S. Komaba, Research development on sodium-ion batteries, *Chem. Rev.* 114 (2014) 11636–11682, <https://doi.org/10.1021/cr500192f>.
- [3] C. Delmas, Sodium and sodium-ion batteries: 50 years of research, *Adv. Energy Mater.* 8 (2018), <https://doi.org/10.1002/aenm.201703137>.
- [4] S. Komaba, Sodium-driven rechargeable batteries: An effort towards future energy storage, *Chem. Lett.* 49 (2020) 1507–1516, <https://doi.org/10.1246/cl.200568>.
- [5] R. Usiskin, Y. Lu, J. Popovic, M. Law, P. Balaya, Y.-S. Hu, J. Maier, Fundamentals, status and promise of sodium-based batteries, *Nat. Rev. Mater.* 6 (2021) 1020–1035, <https://doi.org/10.1038/s41578-021-00324-w>.
- [6] C. Zhao, Y. Lu, Y. Li, L. Jiang, X. Rong, Y.-S. Hu, H. Li, L. Chen, Novel methods for sodium-ion battery materials, *Small Methods* 1 (2017), <https://doi.org/10.1002/smt.201600063>.
- [7] M. Ebadi, A. Nasser, M. Carboni, R. Younesi, C.F.N. Marchiori, D. Brandell, C.M. Araujo, Insights into the Li-metal/organic carbonate interfacial chemistry by combined first-principles theory and X-ray photoelectron spectroscopy, *J. Phys. Chem. C* 123 (2018) 347–355, <https://doi.org/10.1021/acs.jpcc.8b07679>.
- [8] Q. Sun, Y. Xiang, Y. Liu, L. Xu, T. Leng, Y. Ye, A. Fortunelli, W.A. Goddard 3rd, T. Cheng, Machine learning predicts the X-ray photoelectron spectroscopy of the solid electrolyte interface of lithium metal battery, *J. Phys. Chem. Lett.* 13 (2022) 8047–8054, <https://doi.org/10.1021/acs.jpcc.2c02222>.
- [9] Y. Yang, R. Fu, H. Huo, NMR and MRI of electrochemical energy storage materials and devices, *Royal Soc. Chem.* (2021), <https://doi.org/10.1039/9781839160097>.
- [10] X. Liu, Z. Liang, Y. Xiang, M. Lin, Q. Li, Z. Liu, G. Zhong, R. Fu, Y. Yang, Solid-state NMR and MRI spectroscopy for Li/Na batteries: Materials, interface, and in situ characterization, *Adv. Mater.* 33 (2021) 2005878, <https://doi.org/10.1002/adma.202005878>.
- [11] K. Gotoh, <sup>23</sup>Na Solid-state NMR analyses for Na-ion batteries and materials, *Batteries & Supercaps* 4 (2021) 1267–1278, <https://doi.org/10.1002/batt.202000295>.
- [12] J.Z. Hu, N.R. Jaegers, M.Y. Hu, K.T. Mueller, In situ and ex situ NMR for battery research, *J. Phys. Condens. Matter* 30 (2018), <https://doi.org/10.1088/1361-648X/aae5b8>.
- [13] M. Mohammadi, A. Jerschow, In situ and operando magnetic resonance imaging of electrochemical cells: A perspective, *J. Magn. Reson.* 308 (2019), <https://doi.org/10.1016/j.jmr.2019.106600>.
- [14] J. Billaud, R.J. Clement, A.R. Armstrong, J. Canales-Vazquez, P. Rozier, C.P. Grey, P.G. Bruce,  $\beta$ -NaMnO<sub>2</sub>: a high-performance cathode for sodium-ion batteries, *J. Am. Chem. Soc.* 136 (2014) 17243–17248, <https://doi.org/10.1021/ja509704t>.
- [15] R.J. Clément, J. Billaud, A. Robert Armstrong, G. Singh, T. Rojo, P.G. Bruce, C.P. Grey, Structurally stable Mg-doped P2-Na<sub>2/3</sub>Mn<sub>1-y</sub>Mg<sub>y</sub>O<sub>2</sub> sodium-ion battery cathodes with high rate performance: insights from electrochemical, NMR and diffraction studies, *Energ. Environ. Sci.* 9 (2016) 3240–3251, <https://doi.org/10.1039/c6ee01750a>.
- [16] X. Liu, W. Zuo, B. Zheng, Y. Xiang, K. Zhou, Z. Xiao, P. Shan, J. Shi, Q. Li, G. Zhong, R. Fu, Y. Yang, P2-Na<sub>0.67</sub>AlxMn1-xO<sub>2</sub>: Cost-effective, stable and high-rate sodium electrodes by suppressing phase transitions and enhancing sodium cation mobility, *Angew. Chem. Int. Ed. Engl.* 58 (2019) 18086–18095, <https://doi.org/10.1002/anie.201911698>.
- [17] W. Zuo, X. Liu, J. Qiu, D. Zhang, Z. Xiao, J. Xie, F. Ren, J. Wang, Y. Li, G.F. Ortiz, W. Wen, S. Wu, M.S. Wang, R. Fu, Y. Yang, Engineering Na<sup>+</sup>-layer spacings to stabilize Mn-based layered cathodes for sodium-ion batteries, *Nat. Commun.* 12 (2021) 4903, <https://doi.org/10.1038/s41467-021-25074-9>.
- [18] D.H.P. Souza, A.M. D'Angelo, T.D. Humphries, C.E. Buckley, M. Paskevicius, Na<sub>2</sub>B<sub>11</sub>H<sub>13</sub> and Na<sub>11</sub>(B<sub>11</sub>H<sub>14</sub>)<sub>3</sub>(B<sub>11</sub>H<sub>13</sub>)<sub>4</sub> as potential solid-state electrolytes for Na-ion batteries, *Dalton Trans.* (2022), <https://doi.org/10.1039/d2dt01943d>.
- [19] Q. Wang, Y. Liao, X. Jin, C. Cheng, S. Chu, C. Sheng, L. Zhang, B. Hu, S. Guo, H. Zhou, Dual honeycomb-superlattice enables double-high activity and reversibility of anion redox for sodium-ion battery layered cathodes, *Angew. Chem. Int. Ed. Engl.* 61 (2022) e202206625.
- [20] W. Zuo, J. Qiu, X. Liu, B. Zheng, Y. Zhao, J. Li, H. He, K. Zhou, Z. Xiao, Q. Li, G.F. Ortiz, Y. Yang, Highly-stable P2-Na<sub>0.67</sub>MnO<sub>2</sub> electrode enabled by lattice tailoring and surface engineering, *Energy Storage Mater.* 26 (2020) 503–512, <https://doi.org/10.1016/j.ensm.2019.11.024>.
- [21] X. Liu, G. Zhong, Z. Xiao, B. Zheng, W. Zuo, K. Zhou, H. Liu, Z. Liang, Y. Xiang, Z. Chen, G.F. Ortiz, R. Fu, Y. Yang, Al and Fe-containing Mn-based layered cathode with controlled vacancies for high-rate sodium ion batteries, *Nano Energy* 76 (2020), <https://doi.org/10.1016/j.nanoen.2020.104997>.
- [22] Y. Xie, E. Gabriel, L. Fan, I. Hwang, X. Li, H. Zhu, Y. Ren, C. Sun, J. Pipkin, M. Dustin, M. Li, Z. Chen, E. Lee, H. Xiong, Role of lithium doping in P2-Na<sub>0.67</sub>Ni<sub>0.33</sub>Mn<sub>0.67</sub>O<sub>2</sub> for sodium-ion batteries, *Chem. Mater.* 33 (2021) 4445–4455, <https://doi.org/10.1021/acs.chemmater.1c00569>.
- [23] Y. Biecher, A. Baux, F. Fauth, C. Delmas, G.R. Goward, D. Carlier, Structure and electronic structure evolution of P2-Na<sub>x</sub>CoO<sub>2</sub> phases from X-ray diffraction and <sup>23</sup>Na magic angle spinning nuclear magnetic resonance, *Chem. Mater.* 34 (2022) 6431–6439, <https://doi.org/10.1021/acs.chemmater.2c01055>.
- [24] Q. Wang, S. Mariyappan, G. Rousse, A.V. Morozov, B. Porcheron, R. Dedryvere, J. Wu, W. Yang, L. Zhang, M. Chakir, M. Avdeev, M. Deschamps, Y.S. Yu, J. Cabana, M.L. Doublet, A.M. Abakumov, J.M. Tarascon, Unlocking anionic redox activity in O3-type sodium 3d layered oxides via Li substitution, *Nat. Mater.* 20 (2021) 353–361, <https://doi.org/10.1038/s41563-020-00870-8>.
- [25] N.S. Grundish, H. Lyu, I.D. Seymour, G. Henkelman, H. Khani, Disrupting sodium ordering and phase transitions in a layered oxide cathode, *J. Electrochem. Soc.* 169 (2022), <https://doi.org/10.1149/1945-7111/ac60eb>.
- [26] Z. Liu, Y.-Y. Hu, M.T. Dunstan, H. Huo, X. Hao, H. Zou, G. Zhong, Y. Yang, C.P. Grey, Local structure and dynamics in the Na ion battery positive electrode material Na<sub>3</sub>V<sub>2</sub>(PO<sub>4</sub>)<sub>2</sub>F<sub>3</sub>, *Chem. Mater.* 26 (2014) 2513–2521, <https://doi.org/10.1021/cm403728w>.
- [27] Y. Liao, C. Li, F. Geng, M. Shen, B. Hu, Na<sub>3</sub>V<sub>2</sub>(PO<sub>4</sub>)<sub>3</sub> revisited: A high-resolution solid-state NMR study, *J. Phys. Chem. C* 125 (2021) 24060–24066, <https://doi.org/10.1021/acs.jpcc.1c06007>.
- [28] S. Ghosh, N. Barman, E. Gonzalez-Correa, M. Mazumder, A. Zaveri, R. Giovine, A. Manche, S.K. Pati, R.J. Clement, P. Senguttuvan, Elucidating the impact of Mg substitution on the properties of NASICON-Na<sub>3+y</sub>V<sub>2-z</sub>Mg<sub>z</sub>(PO<sub>4</sub>)<sub>3</sub> cathodes, *Adv. Funct. Mater.* 31 (2021), <https://doi.org/10.1002/adfm.202105463>.
- [29] R. Liu, Z. Liang, Y. Xiang, W. Zhao, H. Liu, Y. Chen, K. An, Y. Yang, Recognition of V<sup>3+</sup>/V<sup>4+</sup>/V<sup>5+</sup> multielectron reactions in Na<sub>3</sub>V(PO<sub>4</sub>)<sub>2</sub>: A potential high energy density cathode for sodium-ion batteries, *Molecules* 25 (2020), <https://doi.org/10.3390/molecules25041000>.
- [30] Z. Liang, R. Liu, Y. Xiang, J. Zhu, X. Liu, G.F. Ortiz, Y. Yang, Electrochemical investigation of multi-electron reactions in NaVOPO<sub>4</sub> cathode for sodium-ion batteries, *Electrochim. Acta* 351 (2020), <https://doi.org/10.1016/j.electacta.2020.136454>.
- [31] F. Lu, J. Wang, S. Chang, L. He, M. Tang, Q. Wei, S. Mo, X. Kuang, New-type NASICON-Na<sub>4</sub>FeV(PO<sub>4</sub>)<sub>3</sub> cathode with high retention and durability for sodium ion batteries, *Carbon* 196 (2022) 562–572, <https://doi.org/10.1016/j.carbon.2022.05.033>.
- [32] V.C. Wu, R. Giovine, E.E. Foley, J. Finzel, M. Balasubramanian, E. Sebti, E.M. Mozur, A.H. Kwon, R.J. Clément, Unlocking new redox activity in alluaudite cathodes through compositional design, *Chem. Mater.* 34 (2022) 4088–4103, <https://doi.org/10.1021/acs.chemmater.2c00324>.

- [33] T. Partheeban, B. Senthilkumar, V. Aravindan, S. Madhavi, M. Sasidharan, Binary NaCl–NaF and NaCl–LiF flux-mediated growth of mixed-valence ( $V^{3+/4+}$ ) NASICON-type  $Na_3V_2(PO_4)_2F_{2.5}O_{0.5}$  and  $Na_{2.4}Li_{0.6}V_2(PO_4)_2F_{2.5}O_{0.5}$  for highly reversible Na- and Li-ion storage, *ACS Appl. Energy Mater.* 4 (2021) 1387–1397, <https://doi.org/10.1021/acsaem.0c02622>.
- [34] E.E. Foley, A. Wong, R.C. Vincent, A. Manche, A. Zaveri, E. Gonzalez-Correa, G. Menard, R.J. Clement, Probing reaction processes and reversibility in Earth-abundant  $Na_3FeF_6$  for Na-ion batteries, *PCCP* 23 (2021) 20052–20064, <https://doi.org/10.1039/d1cp02763h>.
- [35] Y. Shao, H. Yue, R. Qiao, J. Hu, G. Zhong, S. Wu, M.J. McDonald, Z. Gong, Z. Zhu, W. Yang, Y. Yang, Synthesis and reaction mechanism of novel fluorinated carbon fiber as a high-voltage cathode material for rechargeable Na batteries, *Chem. Mater.* 28 (2016) 1026–1033, <https://doi.org/10.1021/acs.chemmater.5b03762>.
- [36] M. Miroshnikov, K. Kato, G. Babu, N. Kumar, K. Mahankali, E. Hohenstein, H. Wang, S. Satapathy, K.P. Divya, H. Asare, L.M.R. Arava, P.M. Ajayan, G. John, Nature-derived sodium-ion battery: Mechanistic insights into Na-ion coordination within sustainable molecular cathode materials, *ACS Appl. Energy Mater.* 2 (2019) 8596–8604, <https://doi.org/10.1021/acsaem.9b01526>.
- [37] R.J. Clément, D.S. Middlemiss, I.D. Seymour, A.J. Iltott, C.P. Grey, Insights into the nature and evolution upon electrochemical cycling of planar defects in the  $\beta$ - $NaMnO_2$  Na-ion battery cathode: An NMR and first-principles density functional theory approach, *Chem. Mater.* 28 (2016) 8228–8239, <https://doi.org/10.1021/acs.chemmater.6b03074>.
- [38] C. Ma, J. Alvarado, J. Xu, R.J. Clement, M. Kodur, W. Tong, C.P. Grey, Y.S. Meng, Exploring oxygen activity in the high energy P2-type  $Na_{0.78}Ni_{0.23}Mn_{0.69}O_2$  cathode material for Na-ion batteries, *J. Am. Chem. Soc.* 139 (2017) 4835–4845, <https://doi.org/10.1021/jacs.7b00164>.
- [39] R.A. House, U. Maitra, M.A. Perez-Osorio, J.G. Lozano, L. Jin, J.W. Somerville, L. C. Duda, A. Nag, A. Walters, K.J. Zhou, M.R. Roberts, P.G. Bruce, Superstructure control of first-cycle voltage hysteresis in oxygen-redox cathodes, *Nature* 577 (2020) 502–508, <https://doi.org/10.1038/s41586-019-1854-3>.
- [40] L. Yang, L.Y. Kuo, J.M. López del Amo, P.K. Nayak, K.A. Mazzio, S. Maletti, D. Mikhailova, L. Giebeler, P. Kaghazchi, T. Rojo, P. Adelhelm, Structural aspects of P2-type  $Na_{0.67}Mn_{0.6}Ni_{0.2}Li_{0.2}O_2$  (MNL) stabilization by lithium defects as a cathode material for sodium-ion batteries, *Adv. Funct. Mater.* 31 (2021), <https://doi.org/10.1002/adfm.202102939>.
- [41] N. Voronina, M.Y. Shin, H.J. Kim, N. Yaqoob, O. Guillon, S.H. Song, H. Kim, H.D. Lim, H.G. Jung, Y. Kim, H.K. Lee, K.S. Lee, K. Yazawa, K. Gotoh, P. Kaghazchi, S. T. Myung, Hysteresis-suppressed reversible oxygen-redox cathodes for sodium-ion batteries, *Adv. Energy Mater.* 12 (2022), <https://doi.org/10.1002/aenm.202103939>.
- [42] D.L. Smiley, G.R. Goward, Ex situ  $^{23}Na$  solid-state NMR reveals the local Na-ion distribution in carbon-coated  $Na_2FePO_4F$  during electrochemical cycling, *Chem. Mater.* 28 (2016) 7645–7656, <https://doi.org/10.1021/acs.chemmater.6b02539>.
- [43] C. Li, M. Shen, X. Lou, B. Hu, Unraveling the redox couples of VIII/VIV mixed-valent  $Na_3V_2(PO_4)_2O_{1.6}F_{1.4}$  cathode by parallel-mode EPR and in situ/ex situ NMR, *J. Phys. Chem. C* 122 (2018) 27224–27232, <https://doi.org/10.1021/acs.jpcc.8b09151>.
- [44] Q. Li, Z. Liu, F. Zheng, R. Liu, J. Lee, G.L. Xu, G. Zhong, X. Hou, R. Fu, Z. Chen, K. Amine, J. Mi, S. Wu, C.P. Grey, Y. Yang, Identifying the structural evolution of the sodium ion battery  $Na_2FePO_4F$  cathode, *Angew. Chem. Int. Ed. Engl.* 57 (2018) 11918–11923, <https://doi.org/10.1002/anie.201805555>.
- [45] M. Hadouchi, N. Yaqoob, P. Kaghazchi, M. Tang, J. Liu, P. Sang, Y. Fu, Y. Huang, J. Ma, Fast sodium intercalation in  $Na_{3.41}E_{0.59}FeV(PO_4)_3$ : A novel sodium-deficient NASICON cathode for sodium-ion batteries, *Energy Storage Mater.* 35 (2021) 192–202, <https://doi.org/10.1016/j.ensm.2020.11.010>.
- [46] M.M. Doeff, Y.P. Ma, S.J. Visco, L.C. Dejonghe, Electrochemical insertion of sodium into carbon, *J. Electrochem. Soc.* 140 (1993) L169–L170, <https://doi.org/10.1149/1.12221153>.
- [47] D.A. Stevens, J.R. Dahn, High capacity anode materials for rechargeable sodium-ion batteries, *J. Electrochem. Soc.* 147 (2000) 1271–1273, <https://doi.org/10.1149/1.1393348>.
- [48] H. Au, H. Alptekin, A.C.S. Jensen, E. Olsson, C.A. O’Keefe, T. Smith, M. Crespo-Ribadeneyra, T.F. Headen, C.P. Grey, Q. Cai, A.J. Drew, M.-M. Titirici, A revised mechanistic model for sodium insertion in hard carbons, *Energy Environ. Sci.* 13 (2020) 3469–3479, <https://doi.org/10.1039/d0ee01363c>.
- [49] A. Aishova, G.T. Park, C.S. Yoon, Y.K. Sun, Cobalt-free high-capacity Ni-rich layered  $Lij[Ni_{0.9}Mn_{0.1}O_2]$  cathode, *Adv. Energy Mater.* 10 (2020), <https://doi.org/10.1002/aenm.201903179>.
- [50] C. Bommier, T.W. Surta, M. Dolgos, X. Ji, New mechanistic insights on Na-ion storage in nongraphitizable carbon, *Nano Lett.* 15 (2015) 5888–5892, <https://doi.org/10.1021/acs.nanolett.5b01969>.
- [51] R. Morita, K. Gotoh, M. Fukunishi, K. Kubota, S. Komaba, N. Nishimura, T. Yumura, K. Deguchi, S. Ohki, T. Shimizu, H. Ishida, Combination of solid state NMR and DFT calculation to elucidate the state of sodium in hard carbon electrodes, *J. Mater. Chem. A* 4 (2016) 13183–13193, <https://doi.org/10.1039/c6ta04273b>.
- [52] M. Anji Reddy, M. Helen, A. Groß, M. Fichtner, H. Euchner, Insight into sodium insertion and the storage mechanism in hard carbon, *ACS Energy Lett.* 3 (2018) 2851–2857, <https://doi.org/10.1021/acsenylett.8b01761>.
- [53] J.M. Stratford, P.K. Allan, O. Pecher, P.A. Chater, C.P. Grey, Mechanistic insights into sodium storage in hard carbon anodes using local structure probes, *Chem. Commun. (Camb.)* 52 (2016) 12430–12433, <https://doi.org/10.1039/c6cc06990h>.
- [54] R. Morita, K. Gotoh, K. Kubota, S. Komaba, K. Hashi, T. Shimizu, H. Ishida, Correlation of carbonization condition with metallic property of sodium clusters formed in hard carbon studied using  $^{23}Na$  nuclear magnetic resonance, *Carbon* 145 (2019) 712–715, <https://doi.org/10.1016/j.carbon.2019.01.080>.
- [55] J.-B. Kim, G.-H. Lee, V.W.-h. Lau, J. Zhang, F. Zou, M. Chen, L. Zhou, K.-W. Nam, Y.-M. Kang, Microstructural Investigation into Na-Ion Storage Behaviors of Cellulose-Based Hard Carbons for Na-Ion Batteries, *The Journal of Physical Chemistry C*, 125 (2021) 14559–14566, [10.1021/acs.jpcc.1c03984](https://doi.org/10.1021/acs.jpcc.1c03984).
- [56] J.M. Stratford, A.K. Kleppe, D.S. Keeble, P.A. Chater, S.S. Meysans, C.J. Wright, J. Barker, M.M. Titirici, P.K. Allan, C.P. Grey, Correlating local structure and sodium storage in hard carbon anodes: Insights from pair distribution function analysis and solid-state NMR, *J. Am. Chem. Soc.* 143 (2021) 14274–14286, <https://doi.org/10.1021/jacs.1c06058>.
- [57] Q. Li, X. Liu, Y. Tao, J. Huang, J. Zhang, C. Yang, Y. Zhang, S. Zhang, Y. Jia, Q. Lin, Y. Xiang, J. Cheng, W. Lv, F. Kang, Y. Yang, Q.H. Yang, Sieving carbons promise practical anodes with extensible low-potential plateaus for sodium batteries, *Natl. Sci. Rev.* 9 (2022) nwac084, <https://doi.org/10.1093/nsr/nwac084>.
- [58] X. Chen, C. Liu, Y. Fang, X. Ai, F. Zhong, H. Yang, Y. Cao, Understanding of the sodium storage mechanism in hard carbon anodes, *Carbon Energy* (2022), <https://doi.org/10.1002/cey2.196>.
- [59] X. Chen, J. Tian, P. Li, Y. Fang, Y. Fang, X. Liang, J. Feng, J. Dong, X. Ai, H. Yang, Y. Cao, An overall understanding of sodium storage behaviors in hard carbons by an “Adsorption-Intercalation/Filling” hybrid mechanism, *Adv. Energy Mater.* 12 (2022), <https://doi.org/10.1002/aenm.202200886>.
- [60] K. Gotoh, H. Maruyama, T. Miyatou, M. Mizuno, K. Urita, H. Ishida, Structure and dynamic behavior of sodium-diglyme complex in the graphite anode of sodium ion battery by  $^2H$  nuclear magnetic resonance, *J. Phys. Chem. C* 120 (2016) 28152–28156, <https://doi.org/10.1021/acs.jpcc.6b10962>.
- [61] N. Leifer, M.F. Greenstein, A. Mor, D. Aurbach, G. Goobes, NMR-detected dynamics of sodium co-intercalation with diglyme solvent molecules in graphite anodes linked to prolonged cycling, *J. Phys. Chem. C* 122 (2018) 21172–21184, <https://doi.org/10.1021/acs.jpcc.8b06089>.
- [62] S.C. Jung, Y.-J. Kang, Y.-K. Han, Origin of excellent rate and cycle performance of  $Na^+$ -solvent cointercalated graphite vs. poor performance of  $Li^+$ -solvent case, *Nano Energy* 34 (2017) 456–462, <https://doi.org/10.1016/j.nanoen.2017.03.015>.
- [63] L. Seidl, N. Bucher, E. Chu, S. Hartung, S. Martens, O. Schneider, U. Stimming, Intercalation of solvated Na-ions into graphite, *Energy Environ. Sci.* 10 (2017) 1631–1642, <https://doi.org/10.1039/c7ee00546f>.
- [64] P.M. Bayley, N.M. Trease, C.P. Grey, Insights into electrochemical sodium metal deposition as probed with in situ  $^{23}Na$  NMR, *J. Am. Chem. Soc.* 138 (2016) 1955–1961, <https://doi.org/10.1021/jacs.5b12423>.
- [65] Y. Xiang, G. Zheng, Z. Liang, Y. Jin, X. Liu, S. Chen, K. Zhou, J. Zhu, M. Lin, H. He, J. Wan, S. Yu, G. Zhong, R. Fu, Y. Li, Y. Yang, Visualizing the growth process of sodium microstructures in sodium batteries by in-situ  $^{23}Na$  MRI and NMR spectroscopy, *Nat. Nanotechnol.* 15 (2020) 883–890, <https://doi.org/10.1038/s41565-020-0749-7>.
- [66] P.K. Allan, J.M. Griffin, A. Darwiche, O.J. Borkiewicz, K.M. Wiaderek, K.W. Chapman, A.J. Morris, P.J. Chupas, L. Monconduit, C.P. Grey, Tracking sodium-antimonide phase transformations in sodium-ion anodes: Insights from operando pair distribution function analysis and solid-state NMR spectroscopy, *J. Am. Chem. Soc.* 138 (2016) 2352–2365, <https://doi.org/10.1021/jacs.5b13273>.
- [67] J.M. Stratford, M. Mayo, P.K. Allan, O. Pecher, O.J. Borkiewicz, K.M. Wiaderek, K.W. Chapman, C.J. Pickard, A.J. Morris, C.P. Grey, Investigating sodium storage mechanisms in tin anodes: A combined pair distribution function analysis, density functional theory, and solid-state NMR approach, *J. Am. Chem. Soc.* 139 (2017) 7273–7286, <https://doi.org/10.1021/jacs.7b01398>.
- [68] M. Mayo, K.J. Griffith, C.J. Pickard, A.J. Morris, Ab initio study of phosphorus anodes for lithium- and sodium-ion batteries, *Chem. Mater.* 28 (2016) 2011–2021, <https://doi.org/10.1021/acs.chemmater.5b04208>.
- [69] L.E. Marbella, M.L. Evans, M.F. Groh, J. Nelson, K.J. Griffith, A.J. Morris, C.P. Grey, Sodiation and desodiation via helical phosphorus intermediates in high-capacity anodes for sodium-ion batteries, *J. Am. Chem. Soc.* 140 (2018) 7994–8004, <https://doi.org/10.1021/jacs.8b04183>.
- [70] R. Morita, K. Gotoh, M. Dabhi, K. Kubota, S. Komaba, K. Tokiwa, S. Arabnejad, K. Yamashita, K. Deguchi, S. Ohki, T. Shimizu, R. Laskowski, H. Ishida, States of thermochemically or electrochemically synthesized  $Na_xP_y$  compounds analyzed by solid state  $^{23}Na$  and  $^{31}P$  nuclear magnetic resonance with theoretical calculation, *J. Power Sources* 413 (2019) 418–424, <https://doi.org/10.1016/j.jpowsour.2018.12.070>.
- [71] A. Haffner, A.K. Hatz, C. Hoch, B.V. Lotsch, D. Jöhrendt, Synthesis and structure of the sodium phosphidosilicate  $Na_2SiP_2$ , *Eur. J. Inorg. Chem.* 2020 (2020) 617–621, <https://doi.org/10.1002/ejic.201901083>.
- [72] M. Zarrabeitia, E. Castillo-Martínez, J.M. López Del Amo, A. Eguía-Barrio, M.A. Muñoz-Márquez, T. Rojo, M. Casas-Cabanas, Towards environmentally friendly Na-ion batteries: Moisture and water stability of  $Na_2Ti_3O_7$ , *J. Power Sources* 324 (2016) 378–387, <https://doi.org/10.1016/j.jpowsour.2016.05.103>.
- [73] M.A. Tsiamtsouri, P.K. Allan, A.J. Pell, J.M. Stratford, G. Kim, R.N. Kerber, P.C.M. M. Magusin, D.A. Jefferson, C.P. Grey, Exfoliation of layered Na-ion anode material  $Na_2Ti_3O_7$  for enhanced capacity and cyclability, *Chem. Mater.* 30 (2018) 1505–1516, <https://doi.org/10.1021/acs.chemmater.7b03753>.

- [74] S. Kajiyama, L. Szabova, K. Sodeyama, H. Iinuma, R. Morita, K. Gotoh, Y. Tateyama, M. Okubo, A. Yamada, Sodium-ion intercalation mechanism in MXene nanosheets, *ACS Nano* 10 (2016) 3334–3341, <https://doi.org/10.1021/acsnano.5b06958>.
- [75] J. van Dinter, S. Indris, A. Bitter, D. Grantz, G. Cibir, M. Etter, W. Bensch, Long-term stable, high-capacity anode material for sodium-ion batteries: Taking a closer look at CrPS<sub>4</sub> from an electrochemical and mechanistic point of view, *ACS Appl. Mater. Interfaces* 13 (2021) 54936–54950, <https://doi.org/10.1021/acscami.1c14980>.
- [76] T. Whewell, V.R. Seymour, K. Griffiths, N.R. Halcovitch, A.V. Desai, R.E. Morris, A.R. Armstrong, J.M. Griffin, A structural investigation of organic battery anode materials by NMR crystallography, *Magn. Reson. Chem.* 60 (2022) 489–503, <https://doi.org/10.1002/mrc.5249>.
- [77] E. Sic, M.M. d'Eriil, K. Schutjajew, M.J. Graczyk-Zajac, H. Breitzke, R. Riedel, M. Oschatz, T. Gutmann, G. Buntkowsky, SiCN ceramics as electrode materials for sodium/sodium ion cells – insights from <sup>23</sup>Na in-situ solid-state NMR, *Batteries & Supercaps* 5 (2022), <https://doi.org/10.1002/batt.202200066>.
- [78] R.N. Putra, M. Halim, G. Ali, S.F. Shaikh, A.M. Al-Enizi, T. Fazal, F. Jan Iftikhar, A. N.S. Saqib, High-rate sodium insertion/extraction into silicon oxycarbide-reduced graphene oxide, *New J. Chem.* 44 (2020) 14035–14040, <https://doi.org/10.1039/d0nj02993a>.
- [79] S. Bublil, N. Leifer, R. Nanda, Y. Elias, M. Fayena-Greenstein, D. Aurbach, G. Goobes, Alumina thin coat on pre-charged soft carbon anode reduces electrolyte breakdown and maintains sodiation sites active in Na-ion battery – Insights from NMR measurements, *J. Solid State Chem.* 298 (2021), <https://doi.org/10.1016/j.jssc.2021.122121>.
- [80] G. Coquil, B. Fraisse, N. Dupré, L. Monconduit, Versatile Si/P system as efficient anode for lithium and sodium batteries: Understanding of an original electrochemical mechanism by a full XRD-NMR study, *ACS Appl. Energy Mater.* 1 (2018) 3778–3789, <https://doi.org/10.1021/acsaem.8b00567>.
- [81] S. Kaushik, K. Matsumoto, Y. Orikasa, M. Katayama, Y. Inada, Y. Sato, K. Gotoh, H. Ando, R. Hagiwara, Vanadium diphosphide as a negative electrode material for sodium secondary batteries, *J. Power Sources* 483 (2021), <https://doi.org/10.1016/j.jpowsour.2020.229182>.
- [82] L. Gao, J. Chen, Y. Liu, Y. Yamauchi, Z. Huang, X. Kong, Revealing the chemistry of an anode-passivating electrolyte salt for high rate and stable sodium metal batteries, *J. Mater. Chem. A* 6 (2018) 12012–12017, <https://doi.org/10.1039/c8ta03436b>.
- [83] L.N. Gao, J.E. Chen, Q.L. Chen, X.Q. Kong, The chemical evolution of solid electrolyte interface in sodium metal batteries, *Sci. Adv.* 8 (2022), <https://doi.org/10.1126/sciadv.abm4606>.
- [84] M.A. Munoz-Marquez, M. Zarrabeitia, E. Castillo-Martinez, A. Eguia-Barrio, T. Rojo, M. Casas-Cabanas, Composition and evolution of the solid-electrolyte interphase in Na<sub>2</sub>Ti<sub>2</sub>O<sub>7</sub> electrodes for Na-ion batteries: XPS and Auger parameter analysis, *ACS Appl Mater Interfaces* 7 (2015) 7801–7808, <https://doi.org/10.1021/acscami.5b01375>.
- [85] J. Sun, L.A. O'Dell, M. Armand, P.C. Howlett, M. Forsyth, Anion-derived solid-electrolyte interphase enables long life Na-ion batteries using superconcentrated ionic liquid electrolytes, *ACS Energy Lett.* 6 (2021) 2481–2490, <https://doi.org/10.1021/acscenergylett.1c00816>.
- [86] M. Forsyth, H. Yoon, F. Chen, H. Zhu, D.R. MacFarlane, M. Armand, P.C. Howlett, Novel Na<sup>+</sup> ion diffusion mechanism in mixed organic-inorganic ionic liquid electrolyte leading to high na<sup>+</sup> transference number and stable, high rate electrochemical cycling of sodium cells, *J. Phys. Chem. C* 120 (2016) 4276–4286, <https://doi.org/10.1021/acs.jpcc.5b11746>.
- [87] K. Biernacka, F. Makhlooghiazad, I. Popov, H. Zhu, J.N. Chotard, L.A. O'Dell, A.P. Sokolov, J.M. Pringle, M. Forsyth, Exploration of phase diagram, structural and dynamic behavior of [HMG][FSI] mixtures with NaFSI across an extended composition range, *Phys. Chem. Chem. Phys.* 24 (2022) 16712–16723, <https://doi.org/10.1039/d2cp01910h>.
- [88] P. Stigliano, C. Ferrara, N. Pianta, A. Gentile, L. Mezzomo, R. Lorenzi, V. Berbenni, R. Ruffo, G.B. Appetecchi, P. Mustarelli, Physicochemical properties of Pyr<sub>13</sub>TFSI-NaTFSI electrolyte for sodium batteries, *Electrochim. Acta* 412 (2022), <https://doi.org/10.1016/j.electacta.2022.140123>.
- [89] C. Fritsch, A.L. Hansen, S. Indris, M. Knapp, H. Ehrenberg, Mechanochemical synthesis of amorphous and crystalline Na<sub>2</sub>P<sub>2</sub>S<sub>6</sub> – elucidation of local structural changes by X-ray total scattering and NMR, *Dalton Trans.* 49 (2020) 1668–1673, <https://doi.org/10.1039/c9dt04777h>.
- [90] J. Zheng, Y. Sun, W. Li, X. Feng, W. Chen, Y. Zhao, Effects of comonomers on the performance of stable phosphonate-based gel terpolymer electrolytes for sodium-ion batteries with ultralong cycling stability, *ACS Appl. Mater. Interfaces* 13 (2021) 25024–25035, <https://doi.org/10.1021/acscami.1c06147>.
- [91] B. Santhoshkumar, M.B. Choudhary, A.K. Bera, S.M. Yusuf, M. Ghosh, B. Bahari, High Na<sup>+</sup> conducting Na<sub>3</sub>Zr<sub>2</sub>Si<sub>2</sub>PO<sub>12</sub>/Na<sub>2</sub>Si<sub>2</sub>O<sub>7</sub> composites as solid electrolytes for Na<sup>+</sup> batteries, *J. Am. Ceram. Soc.* 105 (2022) 5011–5019, <https://doi.org/10.1111/jace.18463>.
- [92] S.R. Keshri, I. Mandal, S. Ganiseti, S. Kasimuthumanian, R. Kumar, A. Gaddam, A. Shelke, T.G. Ajithkumar, N.N. Gosvami, N.M.A. Krishnan, A.R. Allu, Elucidating the influence of structure and Ag<sup>+</sup>-Na<sup>+</sup> ion-exchange on crack-resistance and ionic conductivity of Na<sub>3</sub>Al<sub>1.8</sub>Si<sub>1.65</sub>P<sub>1.8</sub>O<sub>12</sub> glass electrolyte, *Acta Mater.* 227 (2022), <https://doi.org/10.1016/j.actamat.2022.117745>.
- [93] D. Wang, G. Zhong, W.K. Pang, Z. Guo, Y. Li, M.J. McDonald, R. Fu, J.-X. Mi, Y. Yang, Toward understanding the lithium transport mechanism in garnet-type solid electrolytes: Li<sup>+</sup> ion exchanges and their mobility at octahedral/tetrahedral sites, *Chem. Mater.* 27 (2015) 6650–6659, <https://doi.org/10.1021/acs.chemmater.5b02429>.
- [94] S. Ramakumar, C. Deviannapoorani, L. Dhivya, L.S. Shankar, R. Murugan, Lithium garnets: Synthesis, structure, Li<sup>+</sup> conductivity, Li<sup>+</sup> dynamics and applications, *Prog. Mater. Sci.* 88 (2017) 325–411, <https://doi.org/10.1016/j.pmatsci.2017.04.007>.
- [95] M.J. Klenk, S.E. Boeberitz, J. Dai, N.H. Jalarvo, V.K. Peterson, W. Lai, Lithium self-diffusion in a model lithium garnet oxide Li<sub>5</sub>La<sub>3</sub>Ta<sub>2</sub>O<sub>12</sub>: A combined quasi-elastic neutron scattering and molecular dynamics study, *Solid State Ion.* 312 (2017) 1–7, <https://doi.org/10.1016/j.ssi.2017.09.022>.
- [96] Y. Deng, C. Eames, L.H.B. Nguyen, O. Pecher, K.J. Griffith, M. Courty, B. Fleutot, J.-N. Chotard, C.P. Grey, M.S. Islam, C. Masquelier, Crystal structures, local atomic environments, and ion diffusion mechanisms of scandium-substituted sodium superionic conductor (NASICON) solid electrolytes, *Chem. Mater.* 30 (2018) 2618–2630, <https://doi.org/10.1021/acs.chemmater.7b05237>.
- [97] A. Shastri, D. Watson, Q.-P. Ding, Y. Furukawa, S.W. Martin, <sup>23</sup>Na nuclear magnetic resonance study of yNa<sub>2</sub>S + (1 - y)[xSiS<sub>2</sub> + (1-x)PS<sub>5</sub>]/2 glassy solid electrolytes, *Solid State Ion.* 340 (2019), <https://doi.org/10.1016/j.ssi.2019.115013>.
- [98] C. Simari, M. Tuccillo, S. Brutti, I. Nicotera, Sodiated Nafion membranes for sodium metal aprotic batteries, *Electrochim. Acta* 410 (2022), <https://doi.org/10.1016/j.electacta.2022.139936>.
- [99] R. Zetti, S. Lunghammer, B. Gadermaier, A. Boulaoued, P. Johansson, H.M.R. Wilkening, I. Hanzu, High Li<sup>+</sup> and Na<sup>+</sup> conductivity in new hybrid solid electrolytes based on the porous MIL-121 metal organic framework, *Adv. Energy Mater.* 11 (2021), <https://doi.org/10.1002/aenm.202003542>.
- [100] B. Santhoshkumar, P.L. Rao, K.V. Ramanathan, A.K. Bera, S.M. Yusuf, V.R. Hathwar, B. Bahari, Structure and ionic conductivity of Na<sub>3-x</sub>Sc<sub>2</sub>Si<sub>x</sub>P<sub>3-x</sub>O<sub>12</sub> (x=0.0, 0.2, 0.4, 0.8) NASICON materials: A combined neutron diffraction, MAS NMR and impedance study, *Solid State Sci.* 111 (2021), <https://doi.org/10.1016/j.solidstatesciences.2020.106470>.
- [101] M. Klett, M. Giesecke, A. Nyman, F. Hallberg, R.W. Lindstrom, G. Lindbergh, I. Furo, Quantifying mass transport during polarization in a Li ion battery electrolyte by in situ <sup>7</sup>Li NMR imaging, *J. Am. Chem. Soc.* 134 (2012) 14654–14657, <https://doi.org/10.1021/ja305461j>.
- [102] R. Bhattacharyya, B. Key, H. Chen, A.S. Best, A.F. Hollenkamp, C.P. Grey, In situ NMR observation of the formation of metallic lithium microstructures in lithium batteries, *Nat. Mater.* 9 (2010) 504–510, <https://doi.org/10.1038/nmat2764>.
- [103] C. Yu, S. Ganapathy, E. Eck, H. Wang, S. Basak, Z. Li, M. Wagemaker, Accessing the bottleneck in all-solid state batteries, lithium-ion transport over the solid-electrolyte-electrode interface, *Nat. Commun.* 8 (2017) 1086, <https://doi.org/10.1038/s41467-017-01187-y>.
- [104] J.M. Bray, C.L. Doswell, G.E. Pavlovskaya, L. Chen, B. Kishore, H. Au, H. Alptekin, E. Kendrick, M.M. Titirici, T. Meersmann, M.M. Britton, Operando visualisation of battery chemistry in a sodium-ion battery by <sup>23</sup>Na magnetic resonance imaging, *Nat. Commun.* 11 (2020) 2083, <https://doi.org/10.1038/s41467-020-15938-x>.
- [105] G.J. Rees, D. Spencer Jolly, Z. Ning, T.J. Marrow, G.E. Pavlovskaya, P.G. Bruce, Imaging sodium dendrite growth in all-solid-state sodium batteries using <sup>23</sup>Na T<sub>2</sub>-weighted magnetic resonance imaging, *Angew. Chem. Int. Ed. Engl.* 60 (2021) 2110–2115, <https://doi.org/10.1002/anie.202013066>.
- [106] C.P. Grey, N. Dupré, NMR studies of cathode materials for lithium-ion rechargeable batteries, *Chem. Rev.* 104 (2004) 4493–4512, <https://doi.org/10.1021/cr020734p>.
- [107] O. Pecher, J. Carretero-González, K.J. Griffith, C.P. Grey, Materials' methods: NMR in battery research, *Chem. Mater.* 29 (2016) 213–242, <https://doi.org/10.1021/acs.chemmater.6b03183>.
- [108] B. Lee, E. Paek, D. Mitlin, S.W. Lee, Sodium metal anodes: Emerging solutions to dendrite growth, *Chem. Rev.* 119 (2019) 5416–5460, <https://doi.org/10.1021/acs.chemrev.8b00642>.
- [109] C. Bao, B. Wang, P. Liu, H. Wu, Y. Zhou, D. Wang, H. Liu, S. Dou, Solid electrolyte interphases on sodium metal anodes, *Adv. Funct. Mater.* 30 (2020), <https://doi.org/10.1002/adfm.202004891>.
- [110] T. Jenkins, J.A. Alarco, B. Cowie, I.D.R. Mackinnon, Validating the electronic structure of vanadium phosphate cathode materials, *ACS Appl. Mater. Interfaces* 13 (2021) 45505–45520, <https://doi.org/10.1021/acscami.1c12447>.
- [111] H. Huo, Z. Lin, G. Zhong, S. Lou, J. Wang, Y. Ma, C. Dai, Y. Xiong, G. Yin, Y. Yang, The origins of kinetics hysteresis and irreversibility of monoclinic Li<sub>3</sub>V<sub>2</sub>(PO<sub>4</sub>)<sub>3</sub>, *J. Energy Chem.* 67 (2022) 593–603, <https://doi.org/10.1016/j.jechem.2021.09.001>.
- [112] N. Wu, P.-H. Chien, Y. Qian, Y. Li, H. Xu, N.S. Grundish, B. Xu, H. Jin, Y.-Y. Hu, G. Yu, J.B. Goodenough, Enhanced surface interactions enable fast Li<sup>+</sup> conduction in oxide/polymer composite electrolyte, *Angew. Chem. Int. Ed.* 59 (2020) 4131–4137, <https://doi.org/10.1002/anie.201914478>.
- [113] S.G. Greenbaum, NMR studies of ion mobility and association in polyether-based polymer electrolytes, *Polym. Adv. Technol.* 4 (1993) 172–178, <https://doi.org/10.1002/pat.1993.220040217>.
- [114] A.B. Gunnarsdottir, C.V. Amanchukwu, S. Menkin, C.P. Grey, Noninvasive in situ NMR study of “Dead Lithium” formation and lithium corrosion in full-cell lithium metal batteries, *J. Am. Chem. Soc.* 142 (2020) 20814–20827, <https://doi.org/10.1021/jacs.0c10258>.
- [115] A. Marchetti, J. Chen, Z. Pang, S. Li, D. Ling, F. Deng, X. Kong, Understanding surface and interfacial chemistry in functional nanomaterials via solid-state NMR, *Adv. Mater.* 29 (2017), <https://doi.org/10.1002/adma.201605895>.
- [116] S. Haber, M. Leskes, What can we learn from solid state NMR on the electrode-electrolyte interface?, *Adv. Mater.* 30 (2018) 1706496, <https://doi.org/10.1002/adma.201706496>.

- [117] F. Sun, Y. Xiang, Q. Sun, G. Zhong, M.N. Banis, Y. Liu, R. Li, R. Fu, M. Zheng, T.-K. Sham, Y. Yang, X. Sun, X. Sun, Origin of high ionic conductivity of Sc-doped sodium-rich NASICON solid-state electrolytes, *Adv. Funct. Mater.* 31 (2021) 2102129, <https://doi.org/10.1002/adfm.202102129>.
- [118] Y. Jin, N.-J.-H. Kneusels, P.C.M.M. Magusin, G. Kim, E. Castillo-Martínez, L.E. Marbella, R.N. Kerber, D.J. Howe, S. Paul, T. Liu, C.P. Grey, Identifying the structural basis for the increased stability of the solid electrolyte interphase formed on silicon with the additive fluororoethylene carbonate, *J. Am. Chem. Soc.* 139 (2017) 14992–15004, <https://doi.org/10.1021/jacs.7b06834>.
- [119] M.A. Hope, B.L.D. Rinkel, A.B. Gunnarsdóttir, K. Märker, S. Menkin, S. Paul, I.V. Sergeev, C.P. Grey, Selective NMR observation of the SEI–metal interface by dynamic nuclear polarisation from lithium metal, *Nat. Commun.* 11 (2020) 2224, <https://doi.org/10.1038/s41467-020-16114-x>.
- [120] S. Haber, Rosy, A. Saha, O. Brontvein, R. Carmieli, A. Zohar, M. Noked, M. Leskes, Structure and Functionality of an Alkylated  $\text{Li}_x\text{Si}_y\text{O}_z$  Interphase for High-Energy Cathodes from DNP-ssNMR Spectroscopy, *Journal of the American Chemical Society*, 143 (2021) 4694–4704. 10.1021/jacs.1c00215
- [121] S. Haber, M. Leskes, Dynamic nuclear polarization in battery materials, *Solid State Nucl. Magn. Reson.* 117 (2022), <https://doi.org/10.1016/j.ssnmr.2021.101763>.
- [122] E.E. Morgan, H.A. Evans, K. Pilar, C.M. Brown, R.J. Clément, R. Maezono, R. Seshadri, B. Monserrat, A.K. Cheetham, Lattice dynamics in the NASICON  $\text{NaZr}_2(\text{PO}_4)_3$  solid electrolyte from temperature-dependent neutron diffraction, NMR, and Ab initio computational studies, *Chem. Mater.* 34 (2022) 4029–4038, <https://doi.org/10.1021/acs.chemmater.2c00212>.
- [123] C. Wan, S. Xu, M.Y. Hu, R. Cao, J. Qian, Z. Qin, J. Liu, K.T. Mueller, J.-G. Zhang, J. Z. Hu, Multinuclear NMR study of the solid electrolyte interface formed in lithium metal batteries, *ACS Appl. Mater. Interfaces* 9 (2017) 14741–14748, <https://doi.org/10.1021/acsami.6b15383>.
- [124] Y.-C. Hsieh, M. Leißing, S. Nowak, B.-J. Hwang, M. Winter, G. Brunklau, Quantification of dead lithium via in situ nuclear magnetic resonance spectroscopy, *Cell Rep. Phys. Sci.* 1 (2020), <https://doi.org/10.1016/j.xcrp.2020.100139>.
- [125] Y. Xiang, M. Tao, G. Zhong, Z. Liang, G. Zheng, X. Huang, X. Liu, Y. Jin, N. Xu, M. Armand, J.-G. Zhang, K. Xu, R. Fu, Y. Yang, Quantitatively analyzing the failure processes of rechargeable Li metal batteries, *Sci. Adv.* 7 (2021) eabj3423, <https://doi.org/10.1126/sciadv.abj3423>.
- [126] V. Martins, J. Xu, X. Wang, K. Chen, I. Hung, Z. Gan, C. Gervais, C. Bonhomme, S. Jiang, A. Zheng, B.E.G. Lucier, Y. Huang, Higher magnetic fields, finer MOF structural information:  $^{17}\text{O}$  solid-state NMR at 35.2 T, *J. Am. Chem. Soc.* 142 (2020) 14877–14889, <https://doi.org/10.1021/jacs.0c02810>.
- [127] E.N. Basse, P.J. Reeves, I.D. Seymour, C.P. Grey,  $^{17}\text{O}$  NMR spectroscopy in lithium-ion battery cathode materials: challenges and interpretation, *J. Am. Chem. Soc.* 144 (2022) 18714–18729, <https://doi.org/10.1021/jacs.2c02927>.
- [128] R. Pigliapochi, A.J. Pell, I.D. Seymour, C.P. Grey, D. Ceresoli, M. Kaupp, DFT investigation of the effect of spin-orbit coupling on the NMR shifts in paramagnetic solids, *Phys. Rev. B* 95 (2017), <https://doi.org/10.1103/PhysRevB.95.054412>.
- [129] A.J. Pell, G. Pintacuda, C.P. Grey, Paramagnetic NMR in solution and the solid state, *Prog. Nucl. Magn. Reson. Spectrosc.* 111 (2019) 1–271, <https://doi.org/10.1016/j.pnmrs.2018.05.001>.
- [130] M. Lin, X. Liu, Y. Xiang, F. Wang, Y. Liu, R. Fu, J. Cheng, Y. Yang, Unravelling the fast alkali-ion dynamics in paramagnetic battery materials combined with NMR and deep-potential molecular dynamics simulation, *Angew. Chem. Int. Ed.* 60 (2021) 12547–12553, <https://doi.org/10.1002/anie.202102740>.
- [131] M. Lin, J. Xiong, M. Su, F. Wang, X. Liu, Y. Hou, R. Fu, Y. Yang, J. Cheng, A machine learning protocol for revealing ion transport mechanisms from dynamic NMR shifts in paramagnetic battery materials, *Chem. Sci.* 13 (2022) 7863–7872, <https://doi.org/10.1039/d2sc01306a>.
- [132] Q. Chen, H. He, Z. Hou, W. Zhuang, T. Zhang, Z. Sun, L. Huang, Building an artificial solid electrolyte interphase with high-uniformity and fast ion diffusion for ultralong-life sodium metal anodes, *J. Mater. Chem. A* 8 (2020) 16232–16237, <https://doi.org/10.1039/d0ta04715e>.
- [133] Q. Shi, Y. Zhong, M. Wu, H. Wang, H. Wang, High-performance sodium metal anodes enabled by a bifunctional potassium salt, *Angew. Chem. Int. Ed. Engl.* 57 (2018) 9069–9072, <https://doi.org/10.1002/anie.201803049>.
- [134] A.I. Freytag, A.D. Pauric, S.A. Krachkovskiy, G.R. Goward, In situ magic-angle spinning  $^7\text{Li}$  NMR analysis of a full electrochemical lithium-ion battery using a jelly roll cell design, *J. Am. Chem. Soc.* 141 (2019) 13758–13761, <https://doi.org/10.1021/jacs.9b06885>.